RESEARCH ARTICLE SUMMARY

CANCER

Osteoblasts remotely supply lung tumors with cancer-promoting SiglecF^{high} neutrophils

Camilla Engblom,* Christina Pfirschke,* Rapolas Zilionis, Janaina Da Silva Martins, Stijn A. Bos, Gabriel Courties, Steffen Rickelt, Nicolas Severe, Ninib Baryawno, Julien Faget, Virginia Savova, David Zemmour, Jaclyn Kline, Marie Siwicki, Christopher Garris, Ferdinando Pucci, Hsin-Wei Liao, Yi-Jang Lin, Andita Newton, Omar K. Yaghi, Yoshiko Iwamoto, Benoit Tricot, Gregory R. Wojtkiewicz, Matthias Nahrendorf, Virna Cortez-Retamozo, Etienne Meylan, Richard O. Hynes, Marie Demay, Allon Klein, Miriam A. Bredella, David T. Scadden, Ralph Weissleder, Mikael J. Pittet†

INTRODUCTION: Myeloid cells have emerged as key regulators of cancer growth because of their abundance in the tumor stroma in a broad range of cancers, their association with clinical outcome, and their ability to modulate tumor progression. Most tumor-infiltrating myeloid cells derive from circulating precursors, which are produced in distant tissues, and some tumors amplify myeloid cell activity by skewing hematopoiesis toward the myeloid lineage or increasing myeloid cell populations in the periphery. For example, patients across diverse cancer types can present with elevated levels of myeloid progenitor cells in peripheral blood. Additionally, increased numbers of circulating myeloid cells, such as neutrophils, often correlate with poorer clinical outcome. It is therefore important to consider host changes that occur away from the tumor stroma to more fully understand the biological processes underlying tumor growth.

RATIONALE: The bone marrow is a tissue of particular interest as it is the main production site for hematopoietic cells corresponding to all circulating blood lineages in the adult. The marrow contains resident cell components, such as osteoblasts, which not only participate in bone maintenance but also regulate hematopoiesis and immune cell fate. However, our understanding of bone dynamics in the context of cancer (growing at sites distant from the local bone microenvironment) and related immune responses remains limited. To address this knowledge gap, we explored whether a common solid cancer—lung adenocarcinoma—remotely affects bone tissue and how this might shape tumor-associated hematopoietic responses and tumor growth.

RESULTS: We show in different mouse models and in cancer patients (n = 70) that lung adenocarcinomas increase bone stromal activity even in the absence of local metastasis. Animal studies further reveal that the cancer-induced bone phenotype involves bone-resident osteocalcin-expressing (Ocn$^+$) osteoblastic cells. Ocn$^+$ cells affect distant tumor progression because experimentally reducing the number of these cells limits lung tumor growth. Also, Ocn$^+$ cells are required for full-fledged tumor infiltration by a distinct subset of neutrophils that are defined by their high expression of the lectin SiglecF (sialic acid–binding immunoglobulin-like lectin F). Compared to other neutrophils, SiglecF^{high} cells express genes associated with cancer-promoting processes, including angiogenesis, myeloid cell differentiation and recruitment, extracellular matrix remodeling, suppression of T cell responses, and tumor cell proliferation and growth. Additionally, SiglecF^{high} neutrophils have increased reactive oxygen species production, promote macrophage differentiation, and boost tumor progression in vivo. We further report that the soluble receptor for advanced glycation end products (sRAGE) is up-regulated in the circulation of tumor-bearing mice and fosters osteoblastic activity and osteoblast-dependent neutrophil maturation in vitro.

ON OUR WEBSITE

Read the full article at http://dx.doi.org/10.1126/science.aal5081

CONCLUSION: This study identifies systemic cross-talk between lung tumors and bones: Lung tumors can remotely activate Ocn$^+$ osteoblastic cells in bones even in the absence of local metastasis. In turn, these Ocn$^+$ cells supply tumors with SiglecF^{high} neutrophils, which foster cancer progression. The findings bear scientific and therapeutic importance because they reveal contributions of the host systemic environment to tumor growth and they position Ocn$^+$ cells, SiglecF^{high} neutrophils, and sRAGE as candidate clinical biomarkers and possible intervention points for anticancer therapy. ■

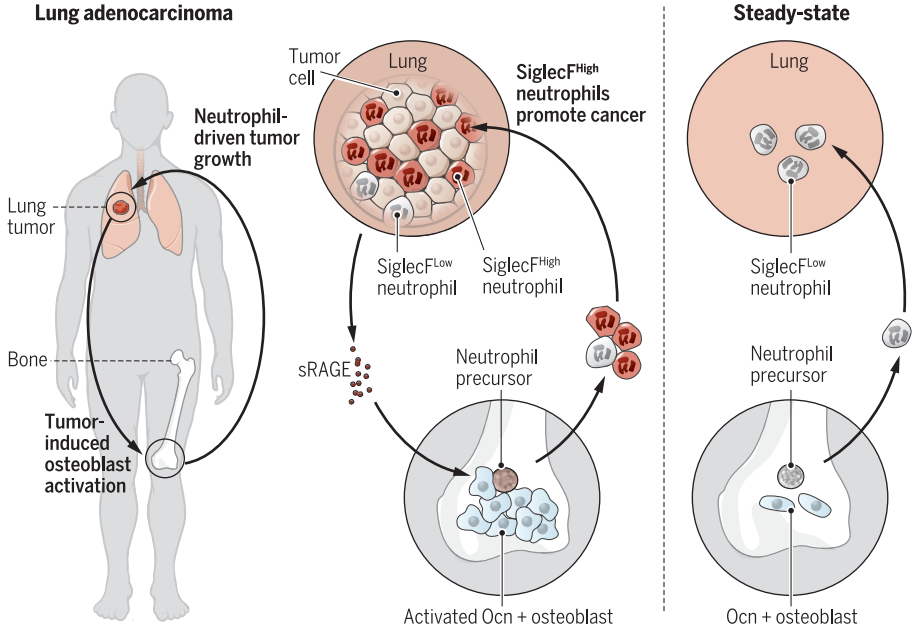

Systemic cross-talk between lung tumors and bones. Lung adenocarcinomas can remotely activate Ocn$^+$ osteoblastic cells in bones even in the absence of local metastasis. In turn, these osteoblasts supply tumors with SiglecF^{high} neutrophils, which exhibit cancer-promoting functions (**left**). By contrast, the bone marrow in steady state only produces SiglecF^{low} neutrophils (**right**).

The list of author affiliations is available in the full article online.
*These authors contributed equally to this work.
†Corresponding author. Email: mpittet@mgh.harvard.edu
Cite this article as C. Engblom *et al.*, *Science* 358, eaal5081 (2017). DOI: 10.1126/science.aal5081

RESEARCH ARTICLE

CANCER

Osteoblasts remotely supply lung tumors with cancer-promoting SiglecF^{high} neutrophils

Camilla Engblom,[1,2]* Christina Pfirschke,[1]* Rapolas Zilionis,[3,4] Janaina Da Silva Martins,[5] Stijn A. Bos,[6] Gabriel Courties,[1] Steffen Rickelt,[7] Nicolas Severe,[8] Ninib Baryawno,[8] Julien Faget,[9] Virginia Savova,[3] David Zemmour,[2,10] Jaclyn Kline,[1] Marie Siwicki,[1,2] Christopher Garris,[1,2] Ferdinando Pucci,[1] Hsin-Wei Liao,[1] Yi-Jang Lin,[1] Andita Newton,[1] Omar K. Yaghi,[1,2] Yoshiko Iwamoto,[1] Benoit Tricot,[1] Gregory R. Wojtkiewicz,[1] Matthias Nahrendorf,[1] Virna Cortez-Retamozo,[1] Etienne Meylan,[9] Richard O. Hynes,[7] Marie Demay,[5] Allon Klein,[3] Miriam A. Bredella,[6] David T. Scadden,[8] Ralph Weissleder,[1,3,6] Mikael J. Pittet[1,6]†

Bone marrow–derived myeloid cells can accumulate within tumors and foster cancer outgrowth. Local immune-neoplastic interactions have been intensively investigated, but the contribution of the systemic host environment to tumor growth remains poorly understood. Here, we show in mice and cancer patients (n = 70) that lung adenocarcinomas increase bone stromal activity in the absence of bone metastasis. Animal studies reveal that the cancer-induced bone phenotype involves bone-resident osteocalcin-expressing (Ocn$^+$) osteoblastic cells. These cells promote cancer by remotely supplying a distinct subset of tumor-infiltrating SiglecF^{high} neutrophils, which exhibit cancer-promoting properties. Experimentally reducing Ocn$^+$ cell numbers suppresses the neutrophil response and lung tumor outgrowth. These observations posit osteoblasts as remote regulators of lung cancer and identify SiglecF^{high} neutrophils as myeloid cell effectors of the osteoblast-driven protumoral response.

Myeloid cells have emerged as key regulators of cancer growth because of their abundance in the tumor stroma in a broad range of cancers, association with patient disease outcome, and ability to modulate tumor progression (*1*–*4*). Most tumor-infiltrating myeloid cells are continuously replenished by circulating precursors, which are produced in distant tissues (*4*, *5*), and some tumors amplify myeloid cell activity by skewing hematopoiesis toward the myeloid lineage or increasing myeloid cell populations in the periphery (*6*–*8*). For example, patients across cancer types present with elevated levels of hematopoietic myeloid progenitor cells in peripheral blood (*9*). Additionally, increased numbers of circulating myeloid cells, such as neutrophils, often correlate with poorer clinical outcome (*10*–*12*). It is therefore important to consider host changes that occur away from the tumor stroma to more fully understand the biological processes underlying tumor growth.

The bone marrow is a tissue of particular interest because it is the main site of hematopoietic cell production for all circulating blood lineages in the adult (*13*). The marrow contains resident cell components that not only participate in bone maintenance but also regulate hematopoiesis and immune cell fate, at least at steady state (*14*–*16*). For example, osteoblasts, which are bone-forming cells, were the first bone-resident cells identified to regulate hematopoiesis (*13*, *14*, *17*). However, our understanding of bone dynamics in the context of cancer (at sites distant from the local bone microenvironment) and related immune responses remains limited. To address this knowledge gap, we explored whether a common solid cancer—lung adenocarcinoma—affects bone tissue and how this might shape tumor-associated hematopoietic responses and distant tumor growth.

Lung tumors modulate bone density in mice and patients

To test whether lung tumors disrupt bone homeostatic activity, we initially used a fluorescent bisphosphonate derivative (OsteoSense-750EX) (*18*) that binds hydroxyapatite minerals in areas of active bone formation and is detectable in vivo by fluorescence-molecular tomography (FMT) (*19*). We considered a mouse model of lung adenocarcinoma in which tumors are induced by intratracheal delivery of Adenovirus-Cre (AdCre), which activates oncogenic *Kras* and deletes the tumor suppressor *Trp53* (hereafter referred to as KP; fig. S1, A to C), and whose growth recapitulates key aspects of the human disease (*20*). We also used the KP1.9 tumor cell line, which derives from KP lung tumor nodules and behaves similarly to its autochthonous counterpart (*21*), and the Lewis lung carcinoma (LLC) cell line, a commonly used murine lung tumor model. In vivo FMT analysis of the femoral-tibial joint (fig. S2A) showed significantly elevated OsteoSense activity in both KP (Fig. 1, A and B) and LLC (Fig. 1C and fig. S2B) lung tumor–bearing mice, when compared to tumor-free controls.

Ex vivo analysis of explanted bones from KP tumor–bearing mice further revealed that this activity extended across all compartments analyzed, including the elbow joint, sternum, ribs, vertebrae, and pelvic bone (fig. S2, C to E). Bone metastases have not been reported for mice bearing KP tumors (*20*), which we confirmed by histology and polymerase chain reaction (PCR)–based methods (fig. S3, A to E). These studies indicate that lung tumors can disrupt bone stromal activity in the absence of local metastasis.

By using confocal microscopy, we also found increased OsteoSense signal in the sternum (Fig. 1D and fig. S4A) and distal femur (fig. S4B) of KP1.9 tumor–bearing mice. The signal's location was separate from vasculature and enriched in areas of active bone remodeling, including the edges of sternebrae, which are associated with areas of increased bone in the sternum (Fig. 1D and fig. S4A). OsteoSense signal was also found in the metaphysis of the femur, which is an area of active trabecular bone formation adjacent to the growth plate (fig. S4B) as well as the epiphysis and diaphysis of the femur (fig. S4B).

These data suggested that KP tumors might influence bone microarchitecture. Accordingly, high-resolution microcomputed tomography (μCT) showed increased trabecular bone volume (Fig. 1E and fig. S5, A to C) and higher mineral density of distal femoral metaphysis (fig. S5D) in mice bearing KP tumors. The same mice also showed more (fig. S5E) and thicker (fig. S5F) trabeculae and decreased space between those trabeculae (fig. S5G). Cortical bone morphology in the femoral mid-diaphysis showed similar tumor-induced phenotypes (fig. S5H). Figure S5I includes a complete tabulation of the μCT results.

To investigate the relevance of our findings to human disease, we examined 35 *KRAS*$^+$ non–small

[1]Center for Systems Biology, Massachusetts General Hospital Research Institute and Harvard Medical School, Boston, MA 02114, USA. [2]Graduate Program in Immunology, Harvard Medical School, Boston, MA 02115, USA. [3]Department of Systems Biology, Harvard Medical School, Boston, MA 02115, USA. [4]Institute of Biotechnology, Vilnius University, Vilnius, LT 10257, Lithuania. [5]Endocrine Unit, Massachusetts General Hospital, Harvard Medical School, Boston, MA 02114, USA. [6]Department of Radiology, Massachusetts General Hospital, MA 02114, USA. [7]Howard Hughes Medical Institute, Koch Institute for Integrative Cancer Research, Massachusetts Institute of Technology, Cambridge, MA 02139, USA. [8]Center for Regenerative Medicine, Massachusetts General Hospital, Boston, MA 02114, USA. [9]Swiss Institute for Experimental Cancer Research, School of Life Sciences, École Polytechnique Fédérale de Lausanne, 1015 Lausanne, Switzerland. [10]Division of Immunology, Department of Microbiology and Immunobiology, Harvard Medical School, Boston, MA 02115, USA.
*These authors contributed equally to this work.
†Corresponding author. Email: mpittet@mgh.harvard.edu

cell lung cancer (NSCLC) patients who had undergone noncontrast chest computed tomography (CT) before cancer therapy and did not have osseous metastases. These patients were matched by age, sex, body mass index, and smoking status to 35 control individuals who did not have active malignancy or chronic illness and who did not use medications known to affect bone metabolism (table S1). This analysis revealed significantly higher trabecular bone density in the thoracic vertebrae of *KRAS*$^+$ NSCLC patients compared to controls (Fig. 1F and table S1). Similarly, equivalent analysis of 35 KRAS nonmutant NSCLC patients revealed increased bone density compared to their matched controls (Fig. 1G). Thus, lung tumor–induced changes in bone occur in both mice and humans.

Lung tumor–induced bone alterations involve osteoblasts

The bone phenotypes may be explained by altered osteoblast and/or osteoclast activity (*22*). Histological analysis of these cell lineages in the distal femur identified more osteoblasts in KP tumor–bearing mice than in tumor-free controls (Fig. 2, A and B). Osteoblasts in tumor-bearing mice also exhibited features of increased activity, including cuboidal shape and association with osteoids (Fig. 2A). Accordingly, the osteoid surface, characterizing newly formed bone, expanded in tumor-bearing mice (fig. S6A). By contrast, osteoclast numbers (fig. S6B) and eroded bone surfaces (fig. S6C) were not significantly different in tumor-bearing mice, although there was a trend for lower osteoclast-related indices compared to tumor-free controls.

To trace osteoblastic lineage cells by genetic means, we generated mice that expressed Cre-driven yellow fluorescent protein (YFP) under the control of the osteoblastic cell reporter osteocalcin (Ocn). Ocn is mainly expressed by mature osteoblasts and constitutes the major noncollagenous protein in the bone (*23*, *24*). We found that Ocn-YFP$^+$ cells expanded in KP tumor–bearing mice when compared to tumor-free controls (Fig. 2C). Femurs of tumor-bearing mice showed increased mineralized bone and bone formation, as assessed by von Kossa staining (Fig. 2D) and dynamic histomorphometry (Fig. 2E and fig. S7).

We next compared the transcriptome of osteocalcin-expressing (Ocn$^+$) cells from tumor-free and lung cancer–bearing mice to ask whether Ocn$^+$ cells in lung cancer–bearing mice acquire unique phenotypes. Specifically, we generated triple transgenic KP-Ocn-GFP (green fluorescent protein) reporter mice (that is, genetically engineered KP mice in which GFP expression is driven by the Ocn promoter) (*20*, *25*), sorted Lin$^-$ CD45$^-$ Ter119$^-$ CD31$^-$ GFP$^+$ (Ocn$^+$) cells from mice with or without tumors, and subjected these cells to RNA sequencing (RNA-seq) analysis (fig. S8A). Control experiments showed that the GFP$^+$ cells expressed 1000-fold higher levels of *Ocn*, *Osteopontin*, *Runx2*, and other osteoblast-associated genes, when compared to CD45$^-$ Ter119$^-$ CD31$^-$ GFP$^-$ cells from the same mice, and thus were highly enriched for Ocn-expressing osteoblasts. RNA-seq analysis identified distinct changes in Ocn$^+$ cells from tumor-bearing mice [101 and 207 genes were significantly up-regulated and down-regulated, respectively; some of these genes were associated with bone phenotypes (fig. S8, B and C)]. For example, Ocn$^+$ cells in tumor-bearing mice up-regulated Fosl2, whose

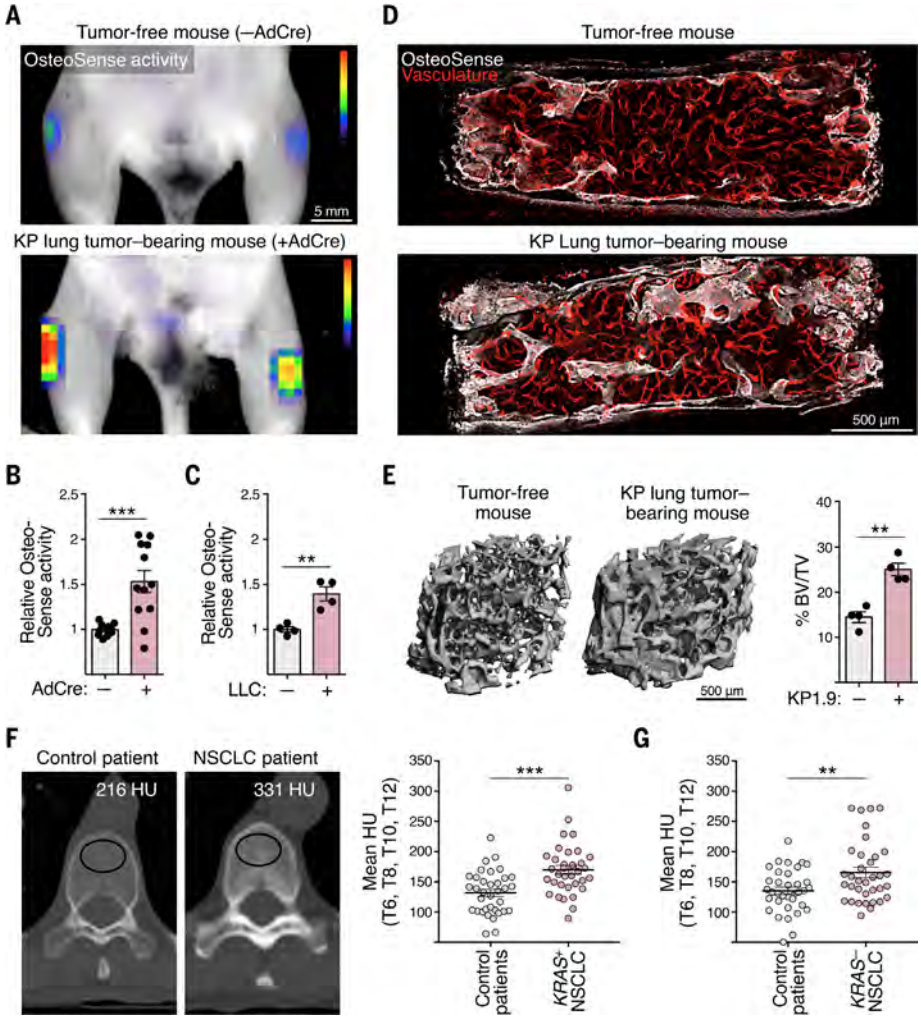

Fig. 1. Lung tumors increase bone density in mouse models and in cancer patients. (**A**) Fluorescence molecular tomography–based detection of OsteoSense signal (marking areas of active bone formation) in the femoral-tibial joint of KP lung tumor–bearing mice compared to their respective age- and sex-matched littermate tumor-free controls. Scale bar, 5 mm. (**B**) Quantification of (A) (n = 10 to 12 femoral-tibial joints per group). (**C**) Detection of OsteoSense signal as in (A) but in LLC lung tumor–bearing mice and their tumor-free controls (n = 4 femoral-tibial joints per group). (**D**) Ex vivo confocal microscopy of representative OsteoSense signal (white) and vasculature signal [red; labeled with anti–Sca-1, anti-CD31, and anti-CD144 monoclonal antibodies (mAbs)] in the sternum of tumor-free mice (top) and KP1.9 lung tumor–bearing mice (bottom). Scale bar, 500 µm. (**E**) Three-dimensional reconstruction of µCT scans (left) and quantification of trabecular bone volume fraction (BV/TV) (right) in the distal femoral metaphysis of KP1.9 lung tumor–bearing and control mice (n = 4 mice per group). Scale bar, 500 µm. (**F**) CT-based trabecular bone density in patients with *KRAS*$^+$ (positive) NSCLC and in control individuals. Left: Representative axial noncontrast CT image of the 10th thoracic vertebra (T10) in a 53-year-old healthy woman who underwent noncontrast chest CT for cough and was found to have no abnormalities (control patient). Middle: A 53-year-old woman with *KRAS*$^+$ NSCLC. Images are presented using the same window and level. The mean trabecular bone density of the region of interest depicted by a black oval (left and middle panels) was calculated in Hounsfield units (HU) for all investigated individuals. Right: Quantitative data from control (n = 35) and *KRAS*$^+$ NSCLC (n = 35) patients. (**G**) As in (F), but showing mean trabecular bone density of *KRAS*$^-$ (negative) NSCLC patients (n = 35) and matched controls (n = 35). All figures show means ± SEM. Statistical significance was calculated using an unpaired t test. $^{**}P < 0.01$, $^{***}P < 0.001$.

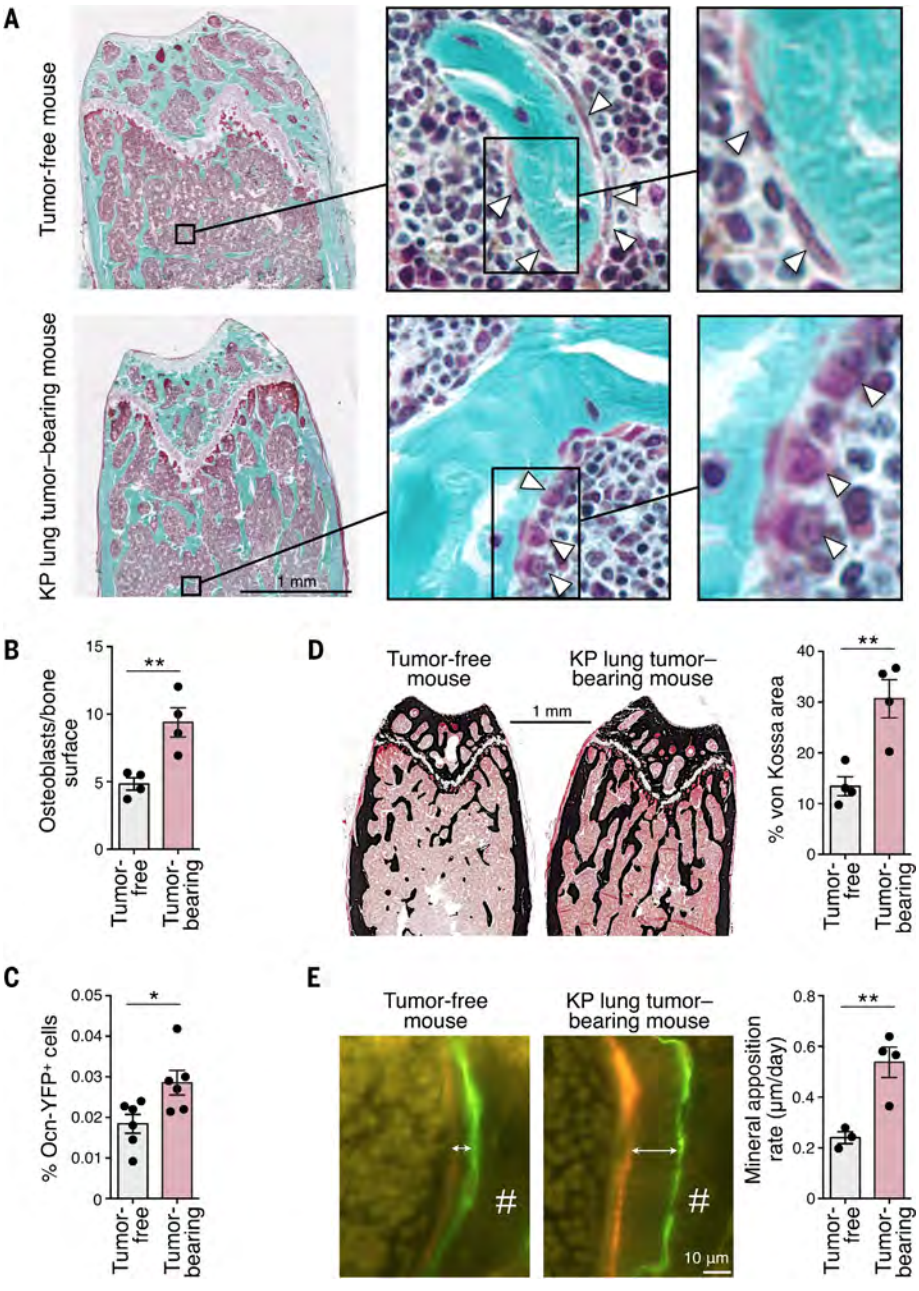

Fig. 2. Lung tumors increase osteoblast activity in mice. (**A**) Representative Goldner's trichrome staining of distal femur sections from a tumor-free mouse (top) and a KP lung tumor–bearing mouse (bottom) (n = 4 mice per group). Osteoblasts are indicated with white arrowheads. Scale bar, 1 mm. See fig. S6 (A to D). (**B**) Number of osteoblasts per bone surface in distal femur trabecular bone from the same mice as in (A) (n = 4 mice per group). (**C**) Flow cytometry–based quantification of the percentage of bone marrow Ocn-YFP$^+$ cells isolated from tumor-free mice and KP lung tumor–bearing $Ocn^{Cre;Yfp}$ mice (n = 6 mice per group). Ocn-YFP$^+$ cells were defined as 7AAD$^-$ (7-aminoactinomycin D–negative) Lin$^-$ CD45$^-$ CD31$^-$ Ter119$^-$ YFP$^+$. (**D**) Representative von Kossa staining (left) and quantification of mineralized bone (% von Kossa area, right) in femurs from the same mice as in (A) (n = 4 mice per group). Scale bar, 1 mm. (**E**) Left: Representative images of bone formation in trabecular bone of femurs from tumor-free mice and KP lung tumor–bearing mice. Double arrows depict distance between sequential injections of calcein (green) and demeclocycline (red). "#" denotes trabecular bone. Scale bar, 10 µm. Right: Quantification of mineral apposition rate (n = 3 to 4 mice per group). See fig. S7 for additional measurements. All figures show means ± SEM. Statistical significance was calculated using an unpaired t test. *P < 0.05, **P < 0.01.

overexpression leads to increased trabecular bone mass (*26*, *27*). Decreased expression of genes, such as *Dlk1* (*28*) and *Ndrg1* (*29*), with ascribed bone inhibitory functions, could also be relevant for the tumor-induced bone activity. On the basis of our combined data, we conclude that KP tumors increase osteoblast numbers, bone formation, and bone mineralization in vivo and induce discrete changes in Ocn$^+$ cell expression of genes related to bone phenotypes.

Ocn$^+$ osteoblasts foster lung tumor growth

To investigate whether bone marrow osteoblastic cells remotely regulate lung cancer growth, we examined tumor progression in $Ocn^{Cre;Dtr}$ mice, a model in which Ocn$^+$ cells can be reduced by diphtheria toxin (DT) injection. We also used $Ocn^{Cre;Dtr/Yfp}$ mice to track Ocn$^+$ cells based on YFP expression. DT treatment did not affect body weight (fig. S9, A and B) but significantly reduced Ocn$^+$ cell numbers, as detected by flow cytometry, immunohistochemistry, in situ microscopy, and bone histomorphometry (fig. S9, C to F). These analyses confirmed that DT treatment of $Ocn^{Cre;Dtr}$ mice resulted in efficient reduction of osteoblastic lineage cells. DT treatment in $Ocn^{Cre;Dtr}$ mice was sufficient to interrupt the progression of established KP lung tumors (Fig. 3, A and B). Control experiments further indicated that tumor reduction required Ocn$^+$ cell targeting because DT treatment did not suppress KP tumor progression in mice lacking the Ocn^{Cre} or DT receptor (DTR) transgenes (Fig. 3A). Suppression of tumor growth was not due to nonspecific DT-induced cell death in the bone marrow because DT targeting of CD169$^+$ bone marrow cells did not suppress KP lung tumor progression in $Cd169^{Dtr}$ mice (fig. S10). These findings indicate that Ocn$^+$ cells affect lung tumor progression.

Ocn$^+$ osteoblasts supply tumor-infiltrating neutrophils

We hypothesized that Ocn$^+$ cells may affect lung cancer growth by supplying specific hematopoietic cells to the tumor microenvironment. We thus compared KP lung tumor immune infiltrates in mice with either unmanipulated or reduced Ocn$^+$ cell numbers. We found similar pools of monocytes, lung macrophages, B cells, and T cells in both cohorts; however, mice with fewer Ocn$^+$ cells showed an about two-fold reduction in CD11b$^+$ Ly-6G$^+$ neutrophils (Fig. 3C and fig. S11). These mice also had more CD49b$^+$ NK1.1$^+$ natural killer (NK) cells (fig. S11), which were likely not required for KP tumor control because NK cell depletion did not restore cancer growth in these mice (fig. S12, A to D). DT did not target neutrophils directly because wild-type mice treated with DT maintained their neutrophil counts (fig. S13, A and B). Also, CD11b$^+$ myeloid cells from $Ocn^{Cre;Dtr}$ mice were not killed by DT in vitro, confirming no functionally relevant DTR expression by these cells (fig. S13, C and D), whereas positive control experiments showed DT's ability to kill DTR$^+$ cells in vitro (fig. S13, E and F).

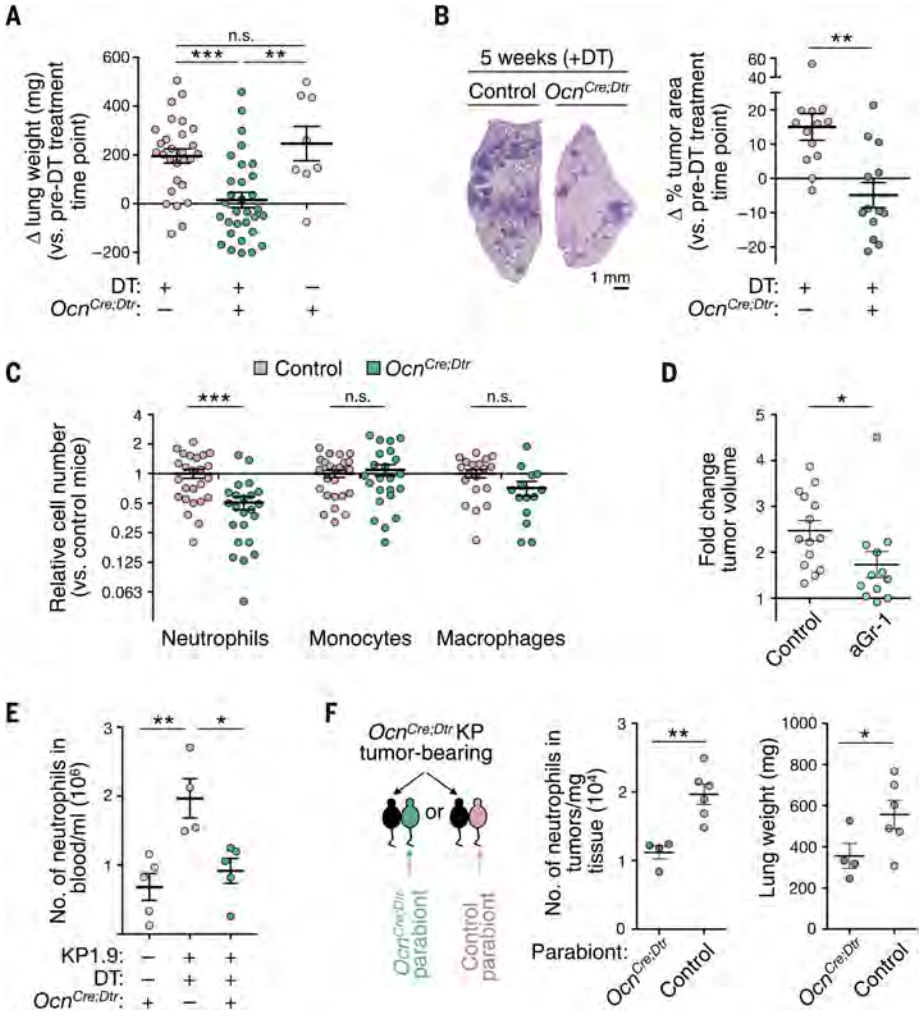

Fig. 3. Ocn$^+$ cells foster a tumor-promoting neutrophil response in mice. (**A**) Comparison of lung weight (proxy of tumor burden) in KP1.9 tumor–bearing mice with reduced numbers of Ocn$^+$ cells (green, *Ocn*$^{Cre;Dtr}$ mice treated with DT) or in tumor-bearing control mice (pink, mice lacking Cre or Dtr and treated with DT). DT was administered 3 weeks after tumor injection, that is, when tumors were established. *Ocn*$^{Cre;Dtr}$ mice that did not receive DT were used as additional controls (gray). Data show delta lung weights (before/after DT treatment) and are pooled from four separate experiments (n = 8 to 31 mice per group). Statistical significance was calculated using one-way analysis of variance (ANOVA) and Tukey's multiple comparisons test. (**B**) Tumor burden in control mice or in mice with reduced numbers of Ocn$^+$ cells. Mice are defined as in (A). Left: Representative hematoxylin and eosin (H&E)–stained lung tissue sections. Scale bar, 1 mm. Right: Quantification of percent change in tumor area after DT treatment. Statistical significance was calculated using an unpaired t test. Data are pooled from three independent experiments (n = 13 mice per group). (**C**) Ex vivo flow cytometry–based evaluation of neutrophils, monocytes, and macrophages in lungs of tumor-bearing control mice or in mice with reduced numbers of Ocn$^+$ cells, as defined in (A). Data were normalized to control (Ocn-sufficient) tumor-bearing mice and pooled from three independent experiments (n = 14 to 25 mice per group). Statistical significance was calculated using multiple t tests. (**D**) Fold change in volume of KP lung tumor nodules after anti–Gr-1 (aGr-1) or isotype mAb treatment versus pretreatment values. Tumors were detected noninvasively by μCT (n = 2 to 3 tumor nodules per mouse, 4 to 5 mice per group). Statistical significance was calculated using an unpaired t test. (**E**) Number of CD11b$^+$ Ly-6G$^+$ neutrophils per milliliter of blood in KP1.9 tumor–bearing control mice (pink) or in mice with reduced numbers of Ocn$^+$ cells (green). Mice are defined as in (A). Mice were analyzed after 3 days of DT treatment (n = 4 to 5 mice per group), and cells were quantified by flow cytometry. Tumor-free *Ocn*$^{Cre;Dtr}$ mice were used as additional controls (gray). Statistical significance was calculated using one-way ANOVA and Tukey's multiple comparisons test. (**F**) Tumor-bearing mice with reduced numbers of Ocn$^+$ cells (mice depicted in black) were parabiosed with mice that had either normal numbers of Ocn$^+$ cells (mouse in pink, control parabiont) or reduced numbers of Ocn$^+$ cells (mouse in green, *Ocn*$^{Cre;Dtr}$ parabiont). Left: Outline of the parabiosis experiments. Middle: Quantification by flow cytometry of lung tumor–infiltrating granulocytes in tumor-bearing *Ocn*$^{Cre;Dtr}$ mice (depicted in black). Right: Lung weight of the same mice (n = 4 to 6 mice per group). Statistical significance was calculated using an unpaired t test. All figures show means ± SEM. *P < 0.05, **P < 0.01, ***P < 0.001.

We next considered whether controlled KP tumor progression in Ocn$^+$ cell–reduced mice involves the altered neutrophil response. In this scenario, removing neutrophils should delay growth of the primary tumor even in the presence of Ocn$^+$ cells. Accordingly, targeting neutrophils with depleting antibodies (Fig. 3D and fig. S14, A and B) significantly suppressed KP lung tumor progression in Ocn$^+$ cell–sufficient mice, as defined by longitudinal and noninvasive μCT monitoring of lung tumor nodules (Fig. 3D).

To assess Ocn$^+$ cells' impact on the tumor-induced systemic neutrophil response, we compared the number of circulating neutrophils in the presence or absence of KP lung tumors when Ocn$^+$ cells were depleted or not. We found that the presence of KP tumors was associated with a significant increase in the number of (CD11b$^+$ Ly-6G$^+$) neutrophils in the blood (Fig. 3E). This response required Ocn$^+$ cells because the number of circulating neutrophils did not increase when Ocn$^+$ cells were depleted. These data indicate that Ocn$^+$ cells are required for the amplification of tumor-associated circulating neutrophils.

To further test this idea, we assessed tumor microenvironments when the circulatory systems of mice were joined by parabiosis. We found that joining osteoblast-reduced mice to osteoblast-sufficient mice increased tumor-infiltrating CD11b$^+$ Ly-6G$^+$ neutrophil numbers in the former by ~ two-fold (Fig. 3F). These neutrophil numbers were comparable to those seen in control (osteoblast-sufficient, nonparabiosed) mice [2.2 ± 0.4–fold; P = n.s. (not significant)]. Tumors in osteoblast-reduced mice grew faster when joined to osteoblast-sufficient parabionts (Fig. 3F) and similarly to tumors in control (osteoblast-sufficient, nonparabiosed) mice (lung weights, 557.1 ± 68.3 and 560.6 ± 29.2 mg, respectively; P = n.s.). Thus, both tumor neutrophil counts and tumor progression were restored in osteoblast-reduced mice when parabiosed to Ocn$^+$ cell–sufficient mice. Combined, these data not only show that Ocn$^+$ cells contribute tumor-infiltrating neutrophils but also suggest that these cells display tumor-promoting functions.

Ocn$^+$ cell–driven neutrophils promote cancer growth

Neutrophils are heterogeneous (*1*), and we therefore wondered whether those supplied by Ocn$^+$ cells have distinct attributes that can accelerate tumor progression. To address this question, we delved deeper into lung neutrophil phenotypes and found that CD11b$^+$ Ly-6G$^+$ cells can be divided into two subsets according to expression levels of the lectin SiglecF (sialic acid–binding

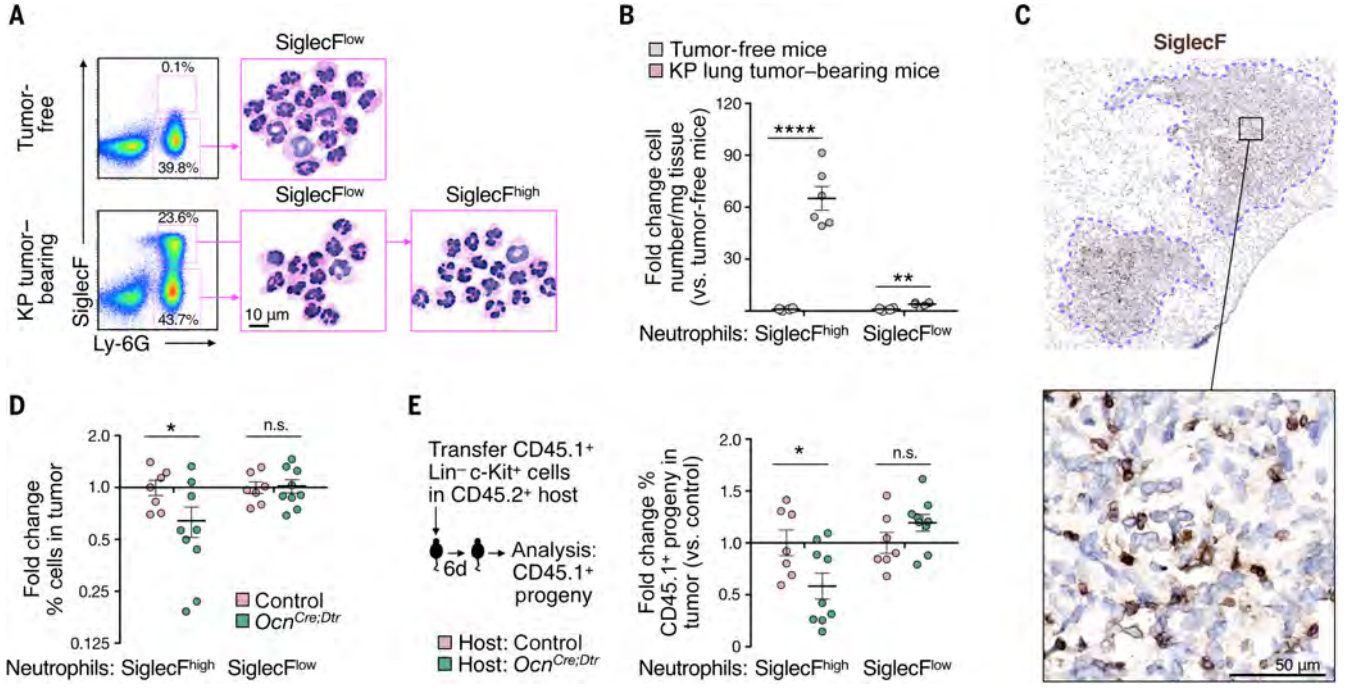

Fig. 4. Ocn$^+$ cell–driven neutrophils show discrete phenotypes. (**A**) Flow cytometry–based detection (left) of Ly-6G$^+$ SiglecF$^{high\ or\ low}$ neutrophils from healthy lung tissue (top) and KP1.9 lung tumors (bottom). Plots are shown for gated live CD45$^+$ CD11b$^+$ cells. Representative cytospin images (right) are from FACS (fluorescence-activated cell sorting)–sorted populations further stained with H&E. Scale bar, 10 μm. (**B**) Fold change Ly-6G$^+$ SiglecF^{high} and Ly-6G$^+$ SiglecF^{low} cell number in lungs from tumor-bearing mice when compared to tumor-free mice. Cells were assessed by flow cytometry (n = 6 mice per group). (**C**) Representative SiglecF mAb staining on cryopreserved KP lung tumor tissue. Tumor areas are highlighted by dotted purple lines. Scale bar, 50 μm. (**D**) Flow cytometry–based quantification of Ly-6G$^+$ SiglecF^{high} and Ly-6G$^+$ SiglecF^{low} cells in tumor-bearing lungs of mice with either preserved Ocn$^+$ cells (pink, control mice treated with DT) or reduced numbers of these cells (green, *Ocn*$^{Cre;Dtr}$ mice treated with DT) (n = 7 to 9 mice per group). (**E**) Ability of CD45.1$^+$ Lin$^-$ c-Kit$^+$ hematopoietic precursors to produce tumor-infiltrating SiglecF^{high} and SiglecF^{low} neutrophils upon transfer into KP tumor–bearing CD45.2$^+$ recipient control mice (pink) or mice with reduced numbers of Ocn$^+$ cells (green). Mice were treated as in (D). Results are shown as fold change relative to control mice. All figures show means ± SEM, and significance values were calculated using multiple t tests. *P < 0.05, **P < 0.01, ****P < 0.0001. Lin., Lineage.

immunoglobulin-like lectin F) (Fig. 4A). The SiglecF^{low} subset appeared in high numbers in healthy lungs and expanded only slightly in lungs from tumor-bearing mice; by contrast, the SiglecF^{high} subset was rare in the healthy tissue but expanded ~70-fold in tumor-bearing lungs (Fig. 4, A and B). The SiglecF^{high}/SiglecF^{low} cell subset ratio positively correlated with KP lung tumor burden (fig. S15, A and B), further indicating that the SiglecF^{high} subset continued to accumulate in growing tumors.

Both the cell surface phenotype and forward/side scatter profiles of the SiglecF^{high} cells closely resembled those of neutrophils and were distinct from those of other myeloid cell types including SiglecF$^+$ eosinophils and SiglecF$^+$ alveolar macrophages (fig. S16). Immunohistochemical SiglecF and Ly-6G staining further revealed the presence of Ly-6G$^+$ and SiglecF^{high} neutrophil–like cells within tumor nodules (Fig. 4C and fig. S17, A and B), suggesting that the SiglecF^{high} neutrophils localize proximal to tumor cells. SiglecF$^+$ cells outside the tumor stroma instead mainly resembled alveolar macrophages on the basis of their morphology and Ly-6G$^-$ phenotype (fig. S17, C to F).

To study whether osteoblasts preferentially contribute SiglecF^{high} lung neutrophils, we quantified both SiglecF^{high} and SiglecF^{low} subsets in tumor-bearing mice with reduced or unchanged Ocn$^+$ cell numbers. We found that Ocn$^+$ cell deficiency significantly reduced the percentage of SiglecF^{high}, but not SiglecF^{low}, neutrophils (Fig. 4D). These data suggest that Ocn$^+$ cells promote SiglecF^{high} neutrophil accumulation in tumors. To further investigate whether SiglecF^{high} neutrophil accumulation in tumors requires Ocn$^+$ cells, we mapped the fate of wild-type donor CD45.1$^+$ c-Kit$^+$ hematopoietic cells upon adoptive transfer into CD45.2$^+$ tumor-bearing recipient mice that had either reduced or unchanged Ocn$^+$ cell numbers. We found that the c-Kit$^+$ donor cells' ability to produce SiglecF^{high} lung neutrophils was impaired in Ocn$^+$ cell–reduced mice (Fig. 4E). These findings indicate that SiglecF^{high} neutrophil accumulation in tumors depends on Ocn$^+$ osteoblastic cells. By contrast, the c-Kit$^+$ donor cells were equally able to produce tumor-infiltrating SiglecF^{low} neutrophils (Fig. 4E), as well as macrophages (fig. S18A) and B cells (albeit at frequencies >25 times lower than myeloid cells; fig. S18B), in Ocn$^+$ cell–reduced and Ocn$^+$ cell–sufficient mice. Donor-derived T cells were very rare or undetectable in the tumor stroma. These findings indicate that KP tumor accumulation of SiglecF^{high} neutrophils, in contrast to other immune cells, depends on Ocn$^+$ cells.

SiglecF^{high} neutrophil profiling reveals cancer-promoting phenotypes

We next asked whether SiglecF^{high} neutrophils in mice have cancer-promoting properties. To this end, we interrogated single-cell transcriptomic data of neutrophils from healthy lungs or KP tumors (table S2). By defining a single-cell SiglecF expression score (table S3; detailed in Materials and Methods), we confirmed that neutrophils in healthy lungs were SiglecF^{low}, whereas tumor tissue contained both SiglecF^{low} and SiglecF^{high} subsets (fig. S19A). We thus compared gene expression of three neutrophil populations: SiglecF^{high} cells in tumor-bearing lung (T-SiglecF^{high}; n = 1502 cells), SiglecF^{low} cells in tumor-bearing lung (T-SiglecF^{low}; n = 273), and SiglecF^{low} cells in healthy lung (H-SiglecF^{low}; n = 4245). Differential gene expression analysis revealed that T-SiglecF^{high} cells substantially diverged from both T-SiglecF^{low} and H-SiglecF^{low} cells (1769 and 1798 differentially expressed genes, respectively; Fig. 5A, table S4, and fig. S19B). T-SiglecF^{low} and H-SiglecF^{low} cells were more similar (123 differentially expressed genes; fig. S19C and table S4).

T-SiglecF^{high} cells selectively up-regulated the expression of genes associated with tumor-promoting processes (Fig. 5B, fig. S19D, and table S5), including angiogenesis (*Vegfa*, *Hif1a*, and *Sema4d*), myeloid cell differentiation and recruitment (*Csf1*, *Ccl3*, and *Mif*), extracellular matrix remodeling (*Adamdec1*, *Adam17*, and various cathepsins), suppression of T cell responses (*Cd274/PDL1*, *Fcgr2b*, and *Havcr2*), and tumor cell proliferation and growth (*Tnf*, *Tgfb1*, and *Il1a*). T-SiglecF^{high} cells also showed decreased expression of genes involved in cytotoxicity (*Cd244*, *Itgal*, and *Fas*) (Fig. 5B). Other genes overexpressed in T-SiglecF^{high} cells included the endoplasmic reticulum stress-response gene and transcription factor *Xbp1* and the short-chain fatty acid receptor *Ffar2* (Fig. 5A); *Xbp1* impairs myeloid antitumor functions (*30*) and positively regulates *Ffar2* expression (*31*). Gene set enrichment analysis indicated up-regulation of genes involved in oxidative phosphorylation, fatty acid metabolism, and glycolysis, suggesting that T-SiglecF^{high} cells undergo a metabolic switch (fig. S20A). Genes involved in Myc signaling and E2F gene targets were also overexpressed, suggesting that T-SiglecF^{high} cells are more proliferative and resistant to apoptosis (fig. S20A). Together, these findings suggest that SiglecF^{high} neutrophils undergo metabolic changes in the tumor microenvironment and are poised to support tumor-promoting functions, including tumor angiogenesis, tumor cell proliferation, extracellular matrix remodeling, and immunosuppressive myeloid cell recruitment.

Tumor-infiltrating neutrophils are replenished by circulating cells. We thus explored whether differentiated SiglecF^{high} neutrophils already exist in the blood of tumor-bearing mice. Specifically, we sorted CD45$^+$ CD11b$^+$ Ly-6G$^+$ neutrophils from the blood of either tumor-free or lung tumor–bearing mice and assessed the expression of several genes that we identified to be selectively up-regulated by tumor-infiltrating SiglecF^{high} neutrophils. This analysis revealed increased expression of transcripts corresponding to *SiglecF*, *Xbp1*, and *Clec4n* (and, to a lesser extent, to *Ltc4s*) in circulating neutrophils from tumor-bearing mice (fig. S21A). In contrast, the expression of *Vegfa* and *Clec5a* was unchanged, and flow cytometry analysis showed comparable expression of SiglecF^{high}-associated cell surface proteins (fig. S21B). These findings suggest that at least some circulating neutrophils acquire molecular features of SiglecF^{high} neutrophils before arrival at the tumor site. However, the acquisition of full-fledged SiglecF^{high} neutrophil phenotypes occurs only after the cells have reached their destination tissue (which likely limits execution of the cells' effector functions to that site).

SiglecF^{high} neutrophils exhibit cancer-promoting functions

Next, we evaluated the functions of SiglecF^{high} compared to SiglecF^{low} neutrophils. First, we tested the capacity of the different neutrophil populations (T-SiglecF^{high}, T-SiglecF^{low}, and H-SiglecF^{low} cells) to produce reactive oxygen species (ROS), which drive diverse protumorigenic inflammatory responses (*6*, *32*, *33*). To this end, we measured intracellular ROS using an imaging probe that becomes fluorescent upon activation by ROS (*6*). SiglecF^{high} neutrophils showed increased ROS activity compared to SiglecF^{low} neutrophils in tumor or tumor-free tissue (Fig. 5C), indicating that ROS activity provided by neutrophils is contributed mainly by the SiglecF^{high} subset.

Second, we assessed the ability of SiglecF^{high} neutrophils to support other tumor-promoting myeloid cells. The neutrophil RNA-seq analysis (Fig. 5A) revealed that T-SiglecF^{high} neutrophils expressed high levels of the mRNA encoding colony-stimulating factor–1 (CSF-1), which is critical for the differentiation of macrophages from monocytes. In addition, monocyte-derived tumor-associated macrophages drive KP tumor growth (*8*). Thus, we hypothesized that SiglecF^{high} neutrophils support cancer progression by promoting the differentiation of tumor-associated macrophages. To test whether T-SiglecF^{high} neutrophils favor macrophage differentiation, we isolated monocytes and myeloid precursors from spleens of tumor-bearing mice and cultured these cells together with either T-SiglecF^{high}, T-SiglecF^{low}, or H-SiglecF^{low} neutrophils. Splenic cells cultured with exogenous CSF-1 (instead of neutrophils) served as a positive control. We found that the presence of T-SiglecF^{high} cells, compared to T-SiglecF^{low} and H-SiglecF^{low} neutrophils, increased the proportion and number (Fig. 5, D and E) of F4/80-expressing cells. These findings indicate that SiglecF^{high} neutrophils promote monocyte differentiation into F4/80$^+$ macrophages.

Third, we asked whether SiglecF^{high} neutrophils promote cancer growth in vivo. To this end, we isolated tumor-associated SiglecF^{high} neutrophils from tumor-bearing mice and, as controls, SiglecF^{low} neutrophils from either tumor-bearing mice or healthy tissue. Each neutrophil population was mixed with KP tumor cells, and the mixture was injected intradermally into mice. We then assessed the relative abilities of these various neutrophil populations to promote KP tumor progression. We found that T-SiglecF^{high} cells accelerated tumor growth compared to either T-SiglecF^{low} or H-SiglecF^{low} cells (Fig. 5F). These data suggest that the KP tumor–promoting effects provided by neutrophils are contributed largely by T-SiglecF^{high} cells. Thus, SiglecF^{high} neutrophils exhibit a tumor-promoting transcriptional profile, have increased ROS production, promote macrophage differentiation, and boost tumor progression in vivo. Overall, our findings indicate that SiglecF^{high} neutrophils have tumor-promoting functions compared to their SiglecF^{low} counterparts.

We next determined whether a mouse SiglecF^{high} neutrophil signature (detailed in Materials and Methods and table S6) might have clinical value. To do this, we analyzed patient tumor transcriptome and survival data (table S7) (*34*, *35*) and asked whether the expression of a SiglecF^{high} neutrophil gene signature was associated with disease outcome in patients with lung adenocarcinoma. A Cox proportional hazards model, controlling for confounding variables, revealed a statistically significant (P = 0.0017) association of the SiglecF^{high} neutrophil signature with worse patient survival (Fig. 5G, fig. S22, and tables S7 and S8). In contrast, the SiglecF^{low} neutrophil signature did not associate with disease outcome in lung cancer patients. The survival of the top 25% versus bottom 25% of SiglecF^{high} and SiglecF^{low} neutrophil signature expressers is shown in Kaplan-Meier plots (Fig. 5G). If these results are confirmed in future studies of independent cohorts of lung adenocarcinoma patients, the T-SiglecF^{high} gene signature may prove to be a valuable biomarker of poorer prognosis.

sRAGE contributes to the osteoblast-induced neutrophil response

The activation of bone marrow–resident cells by distant lung tumors likely involves tumor-induced signals that act over extended distances and stimulate Ocn$^+$ osteoblasts. To begin to address the underlying molecular and cellular mechanisms, we first set up in vitro experiments to define whether the blood of lung tumor–bearing mice contains factors that increase osteoblastic lineage cell activity. We collected serum from either lung tumor–bearing or tumor-free mice and added the serum to bone marrow cells cultured under osteogenic conditions. We then quantified the number of osteoblastic colonies measured by alkaline phosphatase enzymatic staining, as a proxy for osteoblastic activity. As shown in Fig. 6A, serum from tumor-bearing animals significantly increased the number of osteoblastic colonies compared to serum from tumor-free mice. Thus, blood components from tumor-bearing mice are sufficient to promote osteoblastic lineage cells.

To identify specific serum factors that contribute to increased osteoblast activity, we used a protein array to quantify 111 cytokines and growth factors in the blood collected from tumor-bearing or tumor-free mice. We found that the concentration of most of the factors tested was similar in tumor-bearing and tumor-free mice [including the myeloid growth factors G-CSF (granulocyte CSF), GM-CSF (granulocyte-macrophage CSF), and M-CSF (macrophage CSF)], whereas some factors (for example, C1qR1, CCL21, and complement factor D) were slightly enriched in tumor-bearing mice. Notably, the receptor for advanced glycation end products (RAGE) was up-regulated about twofold in the blood of tumor-bearing mice when compared to tumor-free mice (Fig. 6B and fig. S23, A and B). We confirmed this finding using an independent enzyme-linked immunosorbent assay (fig. S23C).

Various ligands can activate membrane-bound RAGE to trigger proinflammatory cascades, a process that has been implicated in several diseases, including diabetes, Alzheimer's disease, and cancer. The circulating form of RAGE, referred to as soluble RAGE (sRAGE), can prevent the binding of ligands, including

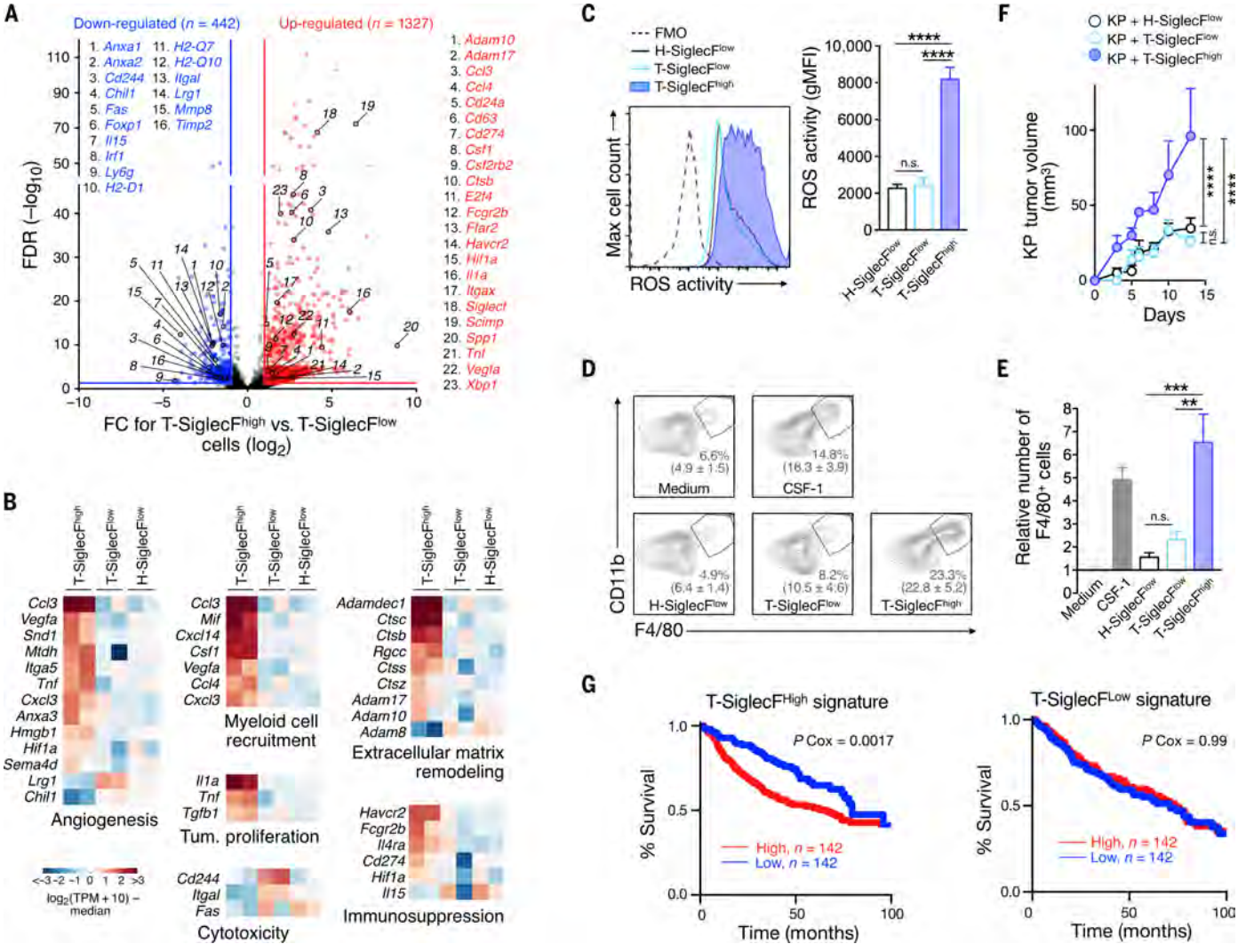

Fig. 5. SiglecF^{high} neutrophils show tumor-promoting phenotypes and functions in mice. (**A**) Volcano plot showing differential gene expression between T-SiglecF^{high} and T-SiglecF^{low} cells. Genes with a false discovery rate (FDR) of <5% and an absolute fold change (FC) of >2 are highlighted in blue and red, denoting down- and up-regulated genes, respectively, in T-SiglecF^{high} cells versus T-SiglecF^{low} cells. Statistical analysis is outlined in Materials and Methods. (**B**) Average expression levels of genes involved in angiogenesis, myeloid cell recruitment, tumor proliferation, cytotoxicity, extracellular matrix remodeling, and immunosuppression in T-SiglecF^{high}, T-SiglecF^{low}, and H-SiglecF^{low} cells. TPM, transcripts per million. (**C**) Representative histogram (left) and quantification of geometric mean fluorescence intensity (gMFI) (right) of ROS activity, measured by rhodamine 123 fluorescence (oxidized Dihydrorhodamine 123) using flow cytometry, in T-SiglecF^{high}, T-SiglecF^{low}, and H-SiglecF^{low} cells (n = 4 to 5 mice per group). (**D**) Representative flow cytometric dot plots showing CD11b^{+}F4/80^{+} macrophages derived from splenic monocytes and cultured with T-SiglecF^{high}, T-SiglecF^{low}, or H-SiglecF^{low} cells (all gated on live CD45^{+} cells). Cultures in medium alone or with CSF-1 were used as negative and positive controls, respectively. Mean macrophage frequencies ± SEM are shown in parentheses. (**E**) Quantification of macrophage numbers as in (D) (four to five replicates per condition). (**F**) KP1.9 tumor growth in mice after tumor cell co-injection with either T-SiglecF^{high}, T-SiglecF^{low}, or H-SiglecF^{low} cells (n = 4 to 5 mice per group). (**G**) Survival (Kaplan-Meier) plots of lung adenocarcinoma patients. Patients were stratified based on high (top 25%) versus low (bottom 25%) expression of a humanized SiglecF^{high} (left) or SiglecF^{low} (right) neutrophil gene signature. P values were calculated using Cox regression method. See Materials and Methods for details. (C to F) Means ± SEM. $^{**}P < 0.01$, $^{***}P < 0.001$, $^{****}P < 0.0001$. Statistical values were calculated using one-way ANOVA (C and E) or two-way ANOVA (F). H, Healthy; T, Tumor.

advanced glycation end products, to the RAGE receptor (*36*). Previous studies have connected sRAGE and RAGE ligands to bone regulation (*37*–*39*). To test the possibility that sRAGE contributes at least in part to increasing osteoblastic activity, we repeated the in vitro osteoblast culture experiment described above, but this time, we specifically asked whether supplementing serum from tumor-free mice with sRAGE was sufficient to stimulate osteoblast activation. This experimental condition significantly increased osteoblastic colony-forming units when compared to control conditions (Fig. 6C).

Finally, we investigated whether sRAGE could stimulate bone marrow neutrophil maturation and whether this process involved stromal osteoblastic cells. Because developing bone marrow neutrophils require up-regulation of CXCR2 expression for release into blood (*1*), we tested neutrophil expression of this chemokine receptor. To this end, we cultured Lin^{-} c-Kit^{+} bone marrow hematopoietic cells with or without the ST2 preosteoblastic cell line and in the presence of increasing doses of exogenous sRAGE (Fig. 6D). This experiment indicated that the presence of sRAGE increases CXCR2 expression on developing neutrophils. Furthermore, we found that CXCR2

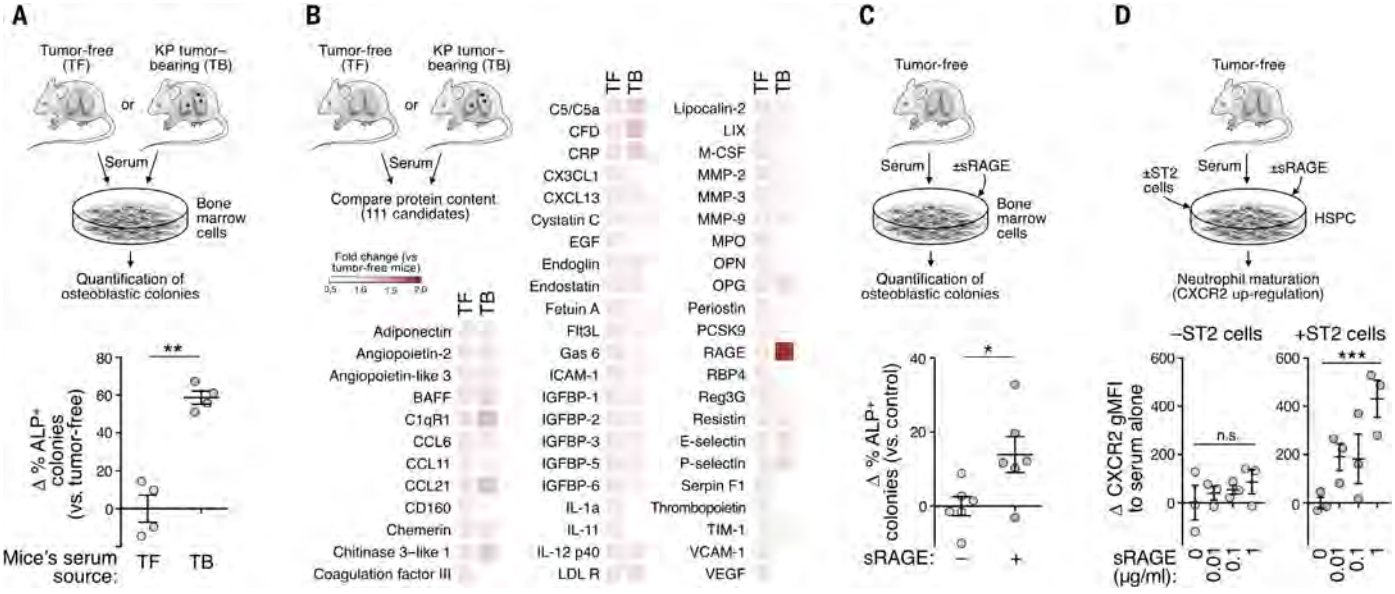

Fig. 6. sRAGE contributes to the osteoblast-induced neutrophil response. (**A**) Bone marrow cells were cultured in osteogenic medium with serum from either tumor-free (TF) or lung tumor–bearing (TB) mice. Osteoblastic colonies were detected by alkaline phosphatase (ALP) staining. Graph shows the change in ALP$^+$ (osteoblastic) colonies upon culture with serum from tumor-bearing mice compared to serum from tumor-free mice (n = 4 replicates per condition). (**B**) Protein content was investigated in the blood of lung tumor–bearing and tumor-free mice using protein arrays. Heat map shows relative protein content that was detectable above background levels and reproducibly altered between two individual protein arrays. The heat map shows pooled results from the two arrays and is normalized to blood from tumor-free mice. Scale, 0.5- to 2.0-fold change. (**C**) Osteoblastic colony formation measured as in (A) but using bone marrow cells exposed or not to sRAGE. Graph shows the change in ALP$^+$ (osteoblastic) colonies upon exposure to sRAGE compared to serum from tumor-free mice alone (n = 6 replicates per condition). (**D**) Flow cytometric evaluation of CXCR2 expression on developing neutrophils derived from bone marrow hematopoietic stem and progenitor cells (HSPCs) of tumor-free mice. The cells were cultured without (left) or with (right) ST2 stromal cells, and with increased amounts of sRAGE (n = 3 replicates per condition).

expression increased only in the presence of bone marrow stromal cells. These preliminary data support the notion that tumor-associated factors can stimulate osteoblastic cells, which in turn regulate immune responses, and suggest sRAGE as an interesting candidate for further investigation.

Discussion

This study identifies systemic cross-talk between lung tumors and bones: Lung adenocarcinomas can remotely activate Ocn$^+$ osteoblasts in bones even in the absence of local metastasis. In turn, these osteoblasts supply tumors with SiglecF^{high} neutrophils, which foster cancer progression. The tumor-promoting functions of SiglecF^{high} neutrophils align with previous experimental data showing that neutrophils can promote cancer in various animal models (*6*, *40*–*45*). The findings also align with human studies, which indicate that a high neutrophil-to-lymphocyte ratio in blood is associated with adverse overall survival in many solid cancers, including that of the lung (*10*), and that lung adenocarcinoma infiltration by neutrophils is strongly linked to poorer clinical outcome (*46*). Both single-cell transcriptomics and functional studies suggest that SiglecF^{high} neutrophils, but not their SiglecF^{low} counterparts, promote primary tumor growth. These data support the idea that tumor-infiltrating neutrophil populations encompass cell subsets with heterogeneous functions (*1*) and suggest new ways to interrogate the neutrophil response to cancer. The phenotype exhibited by SiglecF^{high} neutrophils resembles at least in part that of granulocytic myeloid-derived suppressor cells (MDSCs) (*47*). For example, both granulocytic MDSCs and SiglecF^{high} neutrophils express the CD11b and Ly-6G surface markers, up-regulate proangiogenic factors (for example, *Vegfa*), and produce high levels of ROS (*47*).

Osteoblastic-lineage cells are mostly known for their role in the control of bone formation (*22*, *48*, *49*), but increasing evidence indicates that these cells can also regulate hematopoiesis (*17*, *50*) with reported impacts on both B cell (*51*–*54*) and T cell (*52*, *55*) production at steady state. Also, genetic perturbations of osteoblast-lineage cells deregulate myelopoiesis and can instigate myeloid hematopoietic malignancies (*56*–*58*). Here, we further report that osteoblastic cells can control tumor-infiltrating SiglecF^{high} neutrophils, that is, a discrete immune cell subset of the tumor microenvironment. We did not find evidence that osteoblastic cells control tumor-infiltrating B or T cells, although it is possible that osteoblast-mediated regulation of lymphocytes or other immune cells occurs in other cancer types. Furthermore, the bone marrow is composed of many different resident cell populations including adipocytes, endothelial cells, hematopoietic cells, and neurons, which, together with osteoblasts, form a complex network that is critical to the production, maturation, and egress of hematopoietic populations (*13*). It is conceivable that some cancers affect multiple bone-resident cell populations, which in turn regulate distinct tumor-associated immune events. The study of additional bone marrow–resident cells, for example, with Cre-based models (*13*), may help to capture more fully the complexities of systemic tumor-associated host responses. Additionally, better understanding how lung tumors activate osteoblasts will require further study. Beside the effects of sRAGE identified in this study, it is possible that tumor-bone interactions involve additional components, which remain to be identified.

In accordance with amplified osteoblastic activity in tumor-bearing mice, we observed increased bone density in lung adenocarcinoma patients. This contrasts with the decrease in bone density that is known to occur in patients with some cancer types [for example, those with parathyroid hormone–related protein (PTHrP)–secreting tumors (*59*)] or more broadly in cancer patients after certain anticancer therapies (*60*, *61*). Here, we focused on patients before cancer therapy, and we excluded individuals with chronic conditions (for example, rheumatoid arthritis), medication use (for example, glucocorticoids, bisphosphonates, and previous cancer treatment), paraneoplastic syndromes, and osseous metastases, because these variables can all influence bone density. Because cancer cachexia or smoking can also lead to bone loss, we carefully

matched our lung cancer patients to control individuals with similar body mass index, age, and smoking history. Furthermore, because most lung cancer patients undergo chest CT scans with the administration of intravenous contrast, which can artificially increase bone density measurements (62), we limited our analysis to noncontrast CT scans. Our findings, based on the analysis of 140 individuals, indicate that in NSCLC patients, the primary tumor alters bone metabolism, resulting in increased bone density. It will be important to investigate bone parameters in more patients and in various clinical conditions, because the systemic manifestation of cancer is complex and may vary depending on disease stage, tumor type, and the tumor's secretory profile.

This study underscores the importance of studying cancer as a systemic disease. Interrogating tumor-associated host responses through this lens should be important to fully address fundamental mechanisms of tumor immunity and effects of cancer therapies. Specifically, considering immune cells as critical therapeutic targets, it will be relevant to broadly investigate hematopoietic organs distant from the primary tumor to uncover ways in which cellular and molecular components at those sites control hematopoietic cell production, maturation, and activation in cancer and how these parameters can be manipulated. Given their involvement in shaping tumor progression, our study posits bone marrow–resident Ocn^{+} cells and $SiglecF^{high}$ neutrophils as relevant clinical biomarkers and candidate vantage points for anticancer therapy.

Materials and methods

Mice

Kras$^{LSL\text{-}G12D/WT}$;*p53*$^{Flox/Flox}$ (referred to as KP) mice were used as a conditional mouse model of NSCLC (20) and bred in our laboratory in the C57BL/6 background or in the laboratory of Dr. Meylan. To track and deplete osteoblastic lineage cells by genetic means, we generated mice that expressed Cre-driven yellow fluorescent protein (YFP) under the control of the osteoblastic cell reporter osteocalcin (Ocn) (49, 63, 64). In detail, *Ocn*^{Cre} (*B6N.FVB-Tg(BGLAP-cre)1Clem/J*) transgenic mice were bred to *Rosa*^{Dtr} (*C57BL/6-Gt(ROSA)26Sor*$^{tm1(HBEGF)Awai}$*/J*) and *Rosa*^{Yfp} mice (B6.129X1-*Gt(ROSA)26Sor*$^{tm1(EYFP)Cos}$/J) (Jackson Laboratory) to generate *Ocn*$^{Cre;Dtr}$, *Ocn*$^{Cre;Dtr/Yfp}$ or $Ocn^{Cre;Yfp}$ mice, respectively. Moreover, we generated *KPOcn*^{Gfp} mice by breeding KP mice with *Ocn*$^{Gfp\text{-}topaz}$ (*C57BL6/Tg(BGLAP-Topaz)1Rowe/J*) mice (25). *Cd11c*^{Dtr} mice (B6.FVB-Tg(Itgax-DTR/EGFP)57Lan/J) were obtained from Jackson Laboratory. *Cd169*^{Dtr} transgenic mice (*Siglec1*$^{tm1(HBEGF)Mtka}$) were kindly provided by the Riken Institute (Japan). Wild type and CD45.1 C57BL/6 mice were purchased from Jackson Laboratory. All animal experiments were performed according to approved IACUC guidelines, except experiments in KP mice for anti-Gr-1 antibody (Ab) depletion that were approved by the Veterinary Authority of the Canton de Vaud, Switzerland (license number VD2391) and the Réseau des animaleries lémaniques (RESAL) competent ethic committee.

Following primers were used for genotyping $Ocn^{Cre;Dtr/Yfp}$ and Ocn^{Gfp} mice:

iDTR = WSS-F: 5′-GGCTACTGCTGACTCTCAACATT-3′; DTR-R: TCATGGTGGCGAATTCGAT

Cre = OcnCre-F: CAA ATA GCC CTG GCA GAT TC; OcnCre-R: TGA TAC AAG GGA CAT CTT CC

GFP (Jackson Laboratory) = oIMR0872: TTC ATC TGC ACC ACC G; oIMR1416: TTG AAG AAG ATG GTG CG

Tumor models

Adenovirus-Cre (AdCre) was delivered intratracheally (i.t.) to KP mice as previously described (20, 21). Mice were analyzed for bone or tumor phenotypes 12–14 weeks post-tumor initiation. Tumor burden was scored by measuring post-mortem lung weight and by histological analyses of lung tissue using hematoxylin and eosin (H&E) stainings. For some experiments micro-computed tomography (μCT) was used to monitor tumor burden in the lung. The lung adenocarcinoma cell line KP1.9 was used to induce lung tumors in male wild-type C57BL/6, $Ocn^{Cre;Dtr}$ or $Ocn^{Cre;Yfp}$ mice via intravenous (i.v.) tail vein injection (0.25×10^6 cells in 100 μl PBS). In some osteoblast depletion experiments, mice were killed before DT treatment to quantify the average lung weight (as a proxy for tumor burden). This number was used to calculate the delta lung weight post DT treatment. Male mice with KP1.9 tumors were typically euthanized between 28–41 days after tumor cell injection. Cells of the Lewis lung cancer line (LLC, 1.5×10^6 cells in 150 μl PBS) were injected i.v. into wild-type C57BL/6 mice and the mice were euthanized 32 days post-tumor cell injection. Diphtheria toxin (DT) was used to deplete Ocn^{+} cells in $Ocn^{Cre;Dtr}$ and $Ocn^{Cre;Dtr/Yfp}$ mice; for the detailed depletion protocol see section: In vivo osteoblast depletion.

Cell lines

The KP1.9 cell line, derived from lung tumor nodules of a C57BL/6 KP mouse, was kindly provided by Dr. Zippelius (University Hospital Basel, Switzerland). GFP-positive KP1.9 cells (KP-GFP cell line) were established in our laboratory. The LLC cell line was obtained from ATCC and ST2 cells were kindly provided by Marc Wein (MGH). All cell lines were maintained in Iscove's DMEM media supplemented with 10% fetal bovine serum (FBS) and 1% penicillin/streptomycin.

Patient bone density measurements

The study was conducted using IRB approval (2016P000394/MGH) and complied with HIPAA guidelines with exemption status for individual informed consent. A retrospective search was performed to identify patients with non-small cell lung cancer (NSCLC) who were KRAS positive and KRAS negative, and who had undergone non-contrast chest CT prior to therapy at MGH between 2011 and 2017. Patients with osseous metastases, paraneoplastic syndrome or therapy prior to or at time of chest CT were excluded. Control subjects (referred to as control patients) who had undergone non-contrast chest CT using the same imaging protocols as the patient group were identified and 1:1 matched for sex, age within ±2 years, BMI within ±2 kg/m^2, and smoking (pack-years). Potential controls with active malignancy, significant chronic illness or medication use known to affect bone metabolism were excluded. Trabecular bone density was determined from non-contrast chest CT (16- or 64-MDCT scanner Biograph 16 or 64, Siemens Healthcare; or Discovery CT750HD, GE Healthcare) using an axial slice thickness of 2.5 or 5 mm, 120 kVp and 11–40 mAs. Scans were then reviewed offline on an IMPAX workstation (AGFA Diagnostic Software, version 4, Afga). Circular regions of interest (exemplarily shown in Figure 1F) within trabecular bone of the T6, T8, T10 and T12 vertebral bodies were placed manually, avoiding cortical bone and posterior veins. The mean trabecular bone density of each vertebral body in Hounsfield Units (HU) was determined and an average thoracic trabecular bone density of the four vertebral bodies was calculated.

Fluorescence molecular tomography (FMT)

OsteoSense-750EX (18) was injected retro-orbitally (4nmol/100μl, Perkin Elmer) according to manufacturer's instructions. The mice (for in vivo study) or cleaned bones (for ex vivo investigation) were imaged with FMT no earlier than 4 h and no later than 24 h post OsteoSense injection using an FMT imaging system (VisEn Medical). For in vivo imaging, hair from hind legs and lower abdomen were removed by shaving and chemical depilation. Mice were anaesthetized using isoflurane during the entire scanning procedure. The positioning of the mice relative to the detector were kept consistent throughout the experiments and groups. Detected OsteoSense signal in the femoral-tibial joint (region of interest, ROI) was analyzed using TrueQuant software and normalized against age and sex-matched control values.

Micro-computed tomography (μCT) for lung tumor measurements

Lung tumor volumes were received through repeated μCT measurements and pre- versus post-treatment measurements calculated. Mice were anaesthetized using isoflurane during the entire scanning procedure. Lungs were imaged with a CT (Quantum FX, PerkinElmer) at a 50 μm voxel size, with retrospective respiratory gating. Individual tumor volumes were measured and calculated using the Analyze software (PerkinElmer). Fold change in tumor volume was calculated by dividing post-treatment lung tumor measurements by pretreatment values.

Micro-computed tomography (μCT) for bone microarchitecture

Femurs from KP1.9 tumor-bearing versus age- and sex matched tumor-free controls were dissected out, cleaned, fixed in 10% formalin for 24 h, washed in PBS and transferred to 70% ethanol (EtOH) prior to μCT analysis. Trabecular

bone microarchitecture and cortical bone morphology in the distal femoral metaphysis and mid-diaphysis, respectively, were quantified using a high-resolution desktop micro-tomographic imaging system (μCT40, Scanco Medical AG). The scans were performed using the following settings: 10μm^3 isotropic voxel size, 70 kVp peak x-ray tube intensity, 114 mA x-ray tube current, 200 ms integration time, and were subjected to Gaussian filtration and segmentation. Image acquisition and analysis protocols were performed according to μCT guidelines for the assessment of bone microstructure in rodents (*65*). Trabecular bone was analyzed in a region (1500 μm; 150 transverse slices) extending proximally from 200 μm above the peak of the distal growth plate. A threshold of 339 mgHA/cm^3 was used to segment trabecular bone from soft-tissue and then, trabecular bone volume fraction (BV/TV, %), trabecular thickness (Tb.Th, mm), trabecular number (Tb.N, 1/mm), trabecular separation (Tb.Sp, mm), and trabecular bone mineral density (Tb.BMD, mgHA/ccm) were measured using the Scanco Evaluation program trabecular morphology script. Cortical bone was evaluated in a 500 μm long (50 transverse slices) region at the femoral mid-diaphysis and was segmented using a threshold of 700 mgHA/cm^3 and then analyzed using the Scanco mid-shaft evaluation script to measure total cross-sectional area (Tt.Ar, mm^2), cortical bone area (Ct.Ar, mm^2), medullary area (Ma.Ar, mm^2), bone area fraction (Ct.Ar/Tt.Ar, %), cortical tissue mineral density (Ct.TMD, mgHA/cm^3), cortical thickness (Ct.Th, mm), cortical porosity (%), as well as the maximum, minimum and polar moments of inertia (I_{max}, I_{min}, and J, mm^4).

Histology and immunohistochemistry (IHC)

For histological analysis of tumor burden in mice, lung tissues and femurs were harvested, formaldehyde-fixed and paraffin-embedded following standard procedures and consecutive sections were prepared. Lung tissue sections were stained with H&E to define tumor tissue areas in the lung as described earlier (*21*).

IHC on mouse tissue sections was performed as previously described (*21*). Briefly, mouse lung and bone sections were prepared using a Leica RM2255 rotary microtome (Leica Biosystems), dried at 60°C for 1 h, dewaxed and rehydrated before heat-induced epitoperetrieval (HIER) prior to immunostaining. The sections were incubated in 10mM Tris (pH9.0) or 10mM sodiumcitrate (pH6.0) buffered solution containing 0.05% Tween and, depending on the Ab used, if needed heated at 120°C for 2 min using a pressure cooker. To obtain consistent and reliable staining the LabVision Autostainer 360 (Thermo Fisher Scientific) was used. The sections were pretreated using BLOXALL endogenous enzyme blocking solution (Vector Laboratories) for 10 min to destroy all endogenous peroxidase activity. After blocking with normal goat serum, the sections were incubated with rat anti-mouse Ly-6G (clone 1A8, Biolegend) or anti-mouse osteocalcin (clone M-15, Santa Cruz) monoclonal Abs (mAbs) for 1 h followed by several washes and secondary ImmPRESS polymer detection system (Vector Laboratories) according to the manufacturer's protocol. DAB Quanto (Thermo Fisher Scientific) was applied as substrate and hematoxylin used as counterstain.

Prior to preparation of bone tissue sections, femurs were harvested and cleaned, fixed for 24 h in 10% formalin, washed in PBS and transferred to 70% EtOH. The samples were then decalcified in 14% EDTA for up to two weeks and stored in 70% EtOH until paraffin embedding.

For anti-SiglecF stainings (rat anti-mouse Siglec-F mAb, clone E50-2440, BD Pharmingen), IHC on murine lung tissue of KP tumor-bearing or tumor-free mice was performed on frozen tissue sections. Spleen tissue sections were prepared for reference positive-control stainings. Frozen tissue sections were generated as described before (*21*), air-dried and fixed in acetone (−20°C) for 10 min. The sections were rehydrated and treated as described above, but without HIER.

For histological evaluation of tumor metastases (femur), 10 regions of interest (n = 8) on paraffin-embedded decalcified H&E-stained femur sections were defined at 20x and blindly scored for the presence or absence of tumor cell clusters. Positive control evaluations were done on histological sections from KP tumor-bearing lungs.

For cytospins, SiglecF^{high} neutrophils (CD45$^+$ CD11b$^+$ Ly-6G$^+$ SiglecF$^+$), SiglecF^{low} (CD45$^+$ CD11b$^+$ Ly-6G$^+$ SiglecF$^-$) neutrophils and lung alveolar macrophages (CD45$^+$CD11b$^-$F4/80$^+$ SiglecF$^+$ CD11c$^+$) were FACS sorted from lung tissue of KP tumor-bearing or tumor-free mice based on marker expression using the following anti-mouse mAbs: CD45 (clone 30-F11, Biolegend), Ly-6G (clone 1A8, Biolegend), CD11b (clone M1/70, BD), SiglecF (clone E50-2440, BD), Ly-6C (clone HK1.4, Biolegend), CD11c (clone N418, eBioscience). Cytospins were performed using a Shandon Cytospin 4 centrifuge (Thermo Fisher Scientific). In detail, 5 × 10^4 cells were centrifuged (500 rpm, 3 min) onto Tissue Path Superfrost Plus Gold microscope slides (Thermo Fisher Scientific) and dried overnight at RT. Cytospins were then fixed in 4% formaldehyde-buffered solution and H&E stained following standard procedures.

For all histological sections, image documentation was performed using the NanoZoomer 2.0-RS slide scanner system (Hamamatsu).

Bone histomorphometry

Bone histomorphometric analysis was performed on femurs from KP1.9 tumor-bearing or age and sex-matched tumor-free controls as previously described (*66*). In brief, calcein (20 mg/kg; Sigma) and demeclocycline (50 mg/kg, Sigma) were injected at 9 days and 2 days prior to animal euthanasia, respectively. Dissected, cleaned, formalin-fixed (10%, 24 h) femurs were washed in PBS and transferred to 70% EtOH. Fixed non-decalcified femurs were dehydrated (graded ethanol) and subsequently infiltrated and embedded in methylmethacrylate. Longitudinal sections (5 μM) were cut using a microtome (RM2255, Leica) and stained with Goldner's Trichrome for measurements of cellular parameters and by the method of von Kossa (*67*) to evaluate bone mineralization. Dynamic bone parameters were evaluated on unstained sections by measuring the extent and the distance between double labels using the Osteomeasure analyzing system (Osteometrics Inc.). Measurements were made in the area 200 μm below the growth plate. Quantification of bone parameters was done in a blinded manner. The structural, dynamic and cellular parameters were evaluated using standardized guidelines (*68*).

Confocal microscopy

Confocal microscopy was performed based on a previously published protocol (*69*). The mice were injected with OsteoSense retro-orbitally to label bone (<24 h before mice were sacrificed) and with fluorescently conjugated mAbs (anti-CD31 (clone MEC13.3, Biolegend), anti-CD144 (clone BV13, Biolegend), anti-Sca1 (clone D7, eBioscience)) 30 min prior to euthanasia via cardiac perfusion with PBS and subsequent 4% methanol-free paraformaldehyde (Alfa Aesar). After fixation, the femurs or sternums were quickly dissected out, cleaned of tissue and cut for imaging. In brief, sternum marrow was exposed by cutting longitudinally along the bone and subsequently scanned at 10x (3–4 partially overlapping field of views). Femurs were OCT embedded, frozen at −80°C (>1 h), and marrow tissue was exposed using a cryostat. Z-stack images from femur and sternum were immediately acquired at 2–5 μM steps (Olympus IV100 confocal microscope) and analyzed in FIJI (ImageJ). Non-injected controls or non-fluorescent mice were used as staining controls.

In vivo Gr-1$^+$ cell depletion

Twelve-to-fourteen week-old KP mice were infected i.t. with 1500 Cre-active lentiviral units using a protocol described earlier (*20*). KP mice bearing well-established tumors (identified by μCT) were treated 20 weeks after tumor initiation with anti-Gr-1 mAb (10 mg/kg, clone RB6-8C5, BioXcell) intraperitoneally (i.p.) three times per week for 2 weeks. Neutrophil depletion was validated by tail-vein blood sampling at day 7 followed by flow cytometry analyses of SSC^{hi} Ly-6G$^+$ circulating cells. Control mice were injected with IgG control mAb (10 mg/kg, clone 2A3, Jackson Immunoresearch). At the end of the experiment tumor-bearing lungs were collected and single-cell suspensions were obtained using the GentleMACS tissue octo dissociator (Miltenyi) and an enzymatic digestion mix composed of DMEM, 0.02 mg/ml DNAse I (Sigma) and 1 mg/ml collagenase (Sigma) applied for 35 min at 37°C. Cells were washed with medium then resuspended in PBS supplemented by 2% FBS and 0.5mM EDTA. To obtain single-cell suspensions, cells were passed through 70 μm cell strainer. Cell number was determined and 10^7 cells were used for flow cytometry staining. Cells were first stained with live and dead blue dye (Life Technologies) in PBS containing Fc-Block reagent (Miltenyi) for 20 min at 4°C. After washing, mAb staining (anti-

Ly-6G-FITC, clone RB6-8C5; anti-CD11b-BV711, clone M1/70; anti-Ly-6C-AlexaFluor700, clone HK1.4; anti-CD11c-BV450, clone N418 and anti-CD45-PerCP, clone 30-F11; all from Biolegend) was performed on ice or a 4°C in PBS supplemented with 2% FBS and 0.5mM EDTA for 15 min. All acquisitions were performed using the LSRII SORP (BD), a 5-laser and 18-detector analyzer at the EPFL Flow Cytometry Core Facility. Data analyses were performed using FlowJo X (FlowJo LLC).

In vivo osteoblast depletion

$Ocn^{Cre;Dtr}$, $Ocn^{Cre;Dtr/Yfp}$ and control mice lacking either transgene were treated i.p. with DT (100 µl; 20 µg/kg, Sigma-Aldrich) every other day for 9 days with a total of five injections per mouse. In some experiments, osteoblast depletion was performed for 3 consecutive days using DT. For both DT treatment protocols, osteoblast depletion was verified. Body weight was monitored to control for DT-induced toxicity. Osteoblast depletion was verified using histological evaluation of femurs, IHC for osteocalcin and ex vivo whole mount immunofluorescence of $Ocn^{Cre;Dtr/Yfp}$ mice. Performing in vitro DT titration studies and in vivo cellular stainings using flow cytometry, we ensured that the used DT concentration did not effect the viability of hematopoietic cells in this murine model.

In vivo NK cell depletion

NK cells were depleted in tumor-bearing $Ocn^{Cre;Dtr}$ or control mice performing i.p. injections of anti-NK1.1 Ab (clone PK136, BioXcell, 200µg/mouse, i.p.) every fourth day. The detailed treatment schema is outlined in fig. S12A. NK cell mAb depletion in osteoblast-reduced tumor-bearing mice was evaluated using flow cytometry and was efficient in depleting lung NK cells (defined as $CD49b^+$ $NKp46^+$ cells since the NK1.1 epitope may be masked by the depleting mAb).

In vitro assay to test potential DT-mediated direct effects on hematopoietic cells

Splenocytes from WT, $Cd11c^{Dtr}$ mice, or $Ocn^{Cre;Dtr}$ mice were harvested by gently meshing a spleen through a 40 µm filter. The cells were washed, plated in medium (RPMI, 10% FBS, 1% P/S) and treated with 0, 1, 10, 100, 1000 ng/ml of DT. Cells were harvested after 20 h of incubation at 37°C and stained with mAbs for flow cytometry, see section on flow cytometry for staining procedure.

Parabiosis

In some experiments, parabiosis was used to study the contribution of circulating cells to osteoblast-controlled tumor-infiltrating immune cells. The experimental procedure was performed as previously described (*70*). In brief, one week post-tumor injection, lung tumor-bearing $Ocn^{Cre;Dtr}$ mice were parabiosed to $Ocn^{Cre;Dtr}$ or control mice (lacking either transgene). Both types of parabionts were treated with DT following the procedure described in section: In vivo osteoblast depletion.

Neutrophil single cell RNA-seq

Single-cell RNA sequencing (scRNA-Seq) data were obtained from $CD45^+$ cells collected from either tumor-free or KP tumor-bearing lungs from two independent experimental replicates using droplet microfluidic barcoding technology (inDrops) as previously described (*71*, *72*). To identify single cell expression profiles corresponding to neutrophils among other $CD45^+$ cells, we applied a naive Bayes classifier utilizing immune cell gene expression profiles from the Immgen consortium (*73*). Data from the isolated cell transcriptomes is provided in table S2. Neutrophil transcriptomes were further divided into $SiglecF^{high}$ and $SiglecF^{low}$ cells as follows. Due to the limited sensitivity of scRNA-Seq at the single-cell level, we classified cells based on a composite SiglecF expression score S, among granulocytes (n = 6,020 cells). For each single cell k, we define $S_k = (X_k\text{-}Y_k)$, where $X_k = \sum_{i=1}^{50} r_{k,i}$ and $r_{k,i}$ is the percentile gene expression (dense ranking) of cell k for gene i, for the 50 most correlated genes to SiglecF (Spearman correlation), and $Y_k = \sum_{i=N\text{-}49}^{N} r_{k,i}$ is the corresponding sum of percentiles of the 50 most anticorrelated genes to SiglecF (table S3). As anticipated from FACS data, the distribution of granulocytes by SiglecF expression score was bimodal in tumor, with $SiglecF^{low}$ cells overlapping with healthy granulocytes. By visual inspection of fig. S19A, we set a threshold of −7 to separate between $SiglecF^{high}$ and $SiglecF^{low}$ granulocytes in tumor tissue.

For differential gene expression (DGE) analysis of healthy, tumor $SiglecF^{low}$, and tumor $SiglecF^{high}$ granulocyte populations, we used a parameter-free permutation-based test to calculate p-values, with the difference in means as the test statistic. We accounted for multiple hypothesis testing with a false discovery rate of 5% using the Benjamini-Hochberg procedure (*74*). To be considered for differential gene expression analysis, genes had to be expressed at least by 5% of cells in at least one of the two groups of cells compared. Significantly differentially expressed genes with an absolute fold-change of 2 were selected for further analysis. Genes judged as significant by the permutation test but with a p-value less than the specified accuracy of the permutation test were assigned an approximate p value using a t-test assuming unequal variances for representation on volcano plots.

For gene set enrichment analysis (*75*, *76*), we performed the same pre-filtering as for DGE analysis: only genes expressed by at least 5% of cells in at least on the two groups in a comparison were considered. Then we used the GSEA PreRanked tool (*75*, *76*) on genes ranked by log2 (fold-change) and considered gene sets that were enriched based on an FDR of 25%.

Osteoblast low-input bulk RNA-seq

KP-Ocn^{Gfp} mice were infected with Ad-Cre i.t. and euthanized when high tumor burden was detectable (at 14 weeks post AdCre). All bones were harvested, cleaned and pooled from each single mouse. The bones were crushed gently and the released cells were collected (fraction 1). Red blood cells were lysed using ACK buffer (Lonza) and cells were depleted of mature cells using the lin-depletion kit (Stem cell technologies). In parallel, the bone fragments (fraction 2) were cut finely with scissors, filtered through a 70uM cell strainer (BD), digested for 1h at 37°C (0.25% collagenase type I (Worthington Biochemical Corporation) in FBS), washed and pooled with fraction 1. Ocn-expressing cells were FACS sorted (FACSAria) based on the following parameters: $Lin^-CD45^-CD31^-Ter119^-GFP^+$. Approximately 2000 cells were sorted per mouse into Trizol and frozen at −80°C. RNA was isolated using a Trizol extraction protocol according to the Immgen standard www.immgen.org/Protocols/Total%20RNA%20Extraction%20with%20Trizol.pdf.

Libraries were made following the protocol by Meredith et al. (*77*). RNA was reverse transcribed using ArrayScript (Ambion) using a specific primer containing T7 promoter, the 5′ TruSeq Illumina adapter, a 8-positions with random nucleotide assignment as a unique molecular identifier (UMI), and a oligo-dT sequence. Second-strand synthesis was performed using the mRNA Second strand synthesis module (NEBNext #E6111L). After cDNA size selection using AMPure XP beads (0.8x and 1x, BeckmanCoulter- A63987), the product was amplified via in vitro transcription (MEGAshortscript, Invitrogen) for 12 hours and then fragmented (Magnesium RNA Fragmentation Module, New England Biolabs). 3′ indexing adaptor was ligated (truncated T4 RNA ligase 2 -Enzymatics), reverse-transcribed (Superscript II, Invitrogen), and amplified by PCR for 18 cycles (HiFi hotstart PCR kit, Kapa). cDNA cleanup and size selection were performed on AMPure XP beads. Libraries were quantitated by BioAnalyzer using the Agilent High Sensitivity DNA Kit (Agilent 5067–4626) and qPCR using Kapa library quantification kits, and sequenced on a MiSeq (nano kit) and HiSeq 2500 (rapid mode).

Raw sequencing reads were processed using custom scripts. Read 1 contains the transcript sequence, Read 2 the UMIs. Raw reads were first trimmed using the FASTX-Tollkit v0.0.13 (fastx_trimmer –Q 33) (*78*). Read 2 was trimmed in order to extract the UMI (5-12bp), and Read 1 was trimmed to 30bp eliminate a potential oligo-dT sequence. Reads were filtered for quality (more than 80% of the sequence having a Sanger Phred+33 quality score > 33) using fastq_quality_filter -v -Q 33 -q 20 -p 80. Mapping was performed with Tophat2 to the mm10 mouse transcriptome (*79*) keeping the strand information with the following options: tophat -p 2-library-type fr-firststrand –read- mismatches 5 –read-gap-length 5 –read-edit-dist 5 –nocoverage-search –segment- length 15 –transcriptome-index. Reads mapping at multiple positions were discarded using samtools flag 256 (*80*). Duplicated mapping reads were filtered out using the UMIs with custom R scripts as follows. Reads were first assigned to genes. For each gene, only reads with distinct UMIs were kept. To take into account mutations in UMIs, distinct UMIs but with a Hamming distance of 1 were also collapsed to 1 read. Samples were normalized with DESeq using the estimateSizeFactors

function (*81*). Multiplot studio was used to define differentially expressed genes in Ocn$^+$ cells between tumor-bearing and tumor free mice ($p < 0.05$). Osteoblast RNA-seq data has been deposited under accession number GSE104294.

Survival analysis of lung adenocarcinoma patients

Analyses were performed using tumor microarray data and survival outcome in lung adenocarcinoma patients. Raw microarray CEL files along with patient annotations were obtained from two sources: 1) GSE68465 (*34*) and 2) http://cbio.mskcc.org/public/lung_array_data/ (*35*). CEL files from individual patients were converted into a single expression matrix using ExpressionFileCreator (v12.3, method=MAS5), followed by quantile normalization using the array NCI_U133A_61L as a reference as described before (*34*). Probes were collapsed to gene symbols by selecting the probe with maximum mean expression after excluding probes mapping to multiple gene symbols (*82*). From the list of differentially expressed genes (table S4) between T-SiglecF^{high} and T-SiglecF^{low} neutrophils, we selected genes with a minimum expression of 50 transcripts per million and > 5 times higher expression in T-SiglecF^{high} neutrophils. The resulting 305 mouse genes were mapped to human orthologs using the HCOP tool (www.genenames.org/cgi-bin/hcop), including orthology predictions from Ensembl, NCBI, HGNC, Panther, HomoloGene, OrthoDB, OrthoMCL, OMA, PhylomeDB, TreeFam, Inparanoid, EggNOG. All orthologs were included for mouse genes mapping to multiple human genes. The conversion yielded 302 human orthologs (table S6). Using human patient microarray data, each patient was attributed a 'T-SiglecF^{high} neutrophil signature' value, defined as the sum rank transformed expression of the 302 human orthologs of genes enriched in T-SiglecF^{high} neutrophils in mouse. Here, rank transformation refers to the process by which the expression of gene i in patient j in the microarray data is replaced with the rank for patient j among other patients based on the expression of i (dense ranking). The signature was rescaled to have values from 0 to 1. Cox regression analysis was performed using the T-SiglecF^{high} neutrophil signature, sex, age, T stage, and N stage as predictor variables. Other sample characteristics, which were not documented for a fraction of patients, were used as strata; these included M stage, source of data, histological grade, smoking history, treatment with adjuvant chemotherapy and radiotherapy, tumor relapse, and positive surgical margin (table S7). All predictor variables satisfied the proportional hazards assumption as validated by a Schoenfeld residual tests (cox.zph function in R). To further validate the statistically significant p-value returned by the Cox Hazard test (p value = 0.0017), we randomly sampled 302 genes present in the microarray data, and recorded the number of times a Cox p-value smaller than the one observed was obtained. If the Cox Hazard model is accurate, we would expect approximately 0.17% of random trials to give the observed p-value or less. 7 out 1000 random samplings (0.7%) yielded a Cox p-value <0.0017, indicating a slight underestimate of the p-value by the Cox Hazard model, but nonetheless allowing to reject the null hypothesis of the gene selection being random with $p < 0.01$. The T-SiglecF^{low} gene signature was defined in an analogous way, using the same number (n = 302) of human orthologs of genes most enriched in T-SiglecF^{low} neutrophils. T-SiglecF^{low} neutrophil gene signature showed no significant association with survival. For Kaplan-Meier plots, survival data of top 25% and bottom 25% SiglecF^{high} or SiglecF^{low} signature expressers was used. Survival analysis was performed using the "survival" package in R (*83*) and "Lifelines" package in Python (*84*).

In vivo cell fate mapping

To track the progeny of hematopoietic precursors in tumor-bearing control or Ocn depleted mice, we performed cell fate mapping experiments. We used bead enrichment (Miltenyi) followed by FACS-based sorting of live lineage negative congenic CD45.1 c-Kit$^+$ (CD117) cells (here lineage = B220, CD19, Ter119, CD11c, CD11b, NK1.1, CD49b, CD127, Ly-6G, CD90.2). The purity of the sorted CD45.1$^+$ c-Kit$^+$ cells was above 95%. 2.5×10^5 cells were injected i.v. into tumor-bearing control or Ocn depleted mice (both CD45.2 genotypes) at 29 days post tumor-injection. 7 days post-cKit$^+$ cell transfer, lung tumor tissue was harvested and CD45.1$^+$ immune cell infiltrates were quantified using flow cytometry. Non-injected biological controls, Fluorescence Minus One (FMO)-staining controls and unstained cells were used to analyze the CD45.1$^+$ cell progeny in the tissue.

In vivo tumor cell and neutrophil co-injection experiment

To investigate whether SiglecF^{high} neutrophils are able to support the growth of tumor cells in vivo, we co-injected KP-GFP tumor cells with different neutrophil subpopulations (T-SiglecF^{high}, T-SiglecF^{low} or H-SiglecF^{low}) intradermally (i.d.) to the flank of C57BL/6 mice. Neutrophils were FACS sorted based on cell surface marker expression (CD45$^+$CD11b$^+$Ly-6G$^+$SiglecF$^+$ or SiglecF$^-$) from lungs of KP1.9 tumor-bearing or tumor-free mice as detailed in the Flow cytometry methods section. Tumor cells (2×10^5) and the respective neutrophil population (2×10^5) were mixed in 50 µl 1xPBS before i.d. injection (1:1 ratio). Tumor growth was recorded over time with a digital caliper and tumor volumes defined as $\Pi/6$ x length x width^2.

Ex vivo ROS activity assay

Neutrophils were analyzed ex vivo for their reactive oxygen species (ROS) content. Single cell suspensions were generated from KP tumor-bearing lungs or lungs of tumor-free mice as described in the Flow cytometry methods section. Cells were resuspended in HBSS containing 0.1% BSA followed by FACS antibody surface marker staining for 30min on ice as detailed below. Then cells were washed and resuspended in PBS-EGG buffer (1 mM EDTA, 0.05% gelatin, 0.09% glucose) and 0.5 µM DHR123 probe (Thermo Fisher Scientific) was added for 30 min at 37°C. The reaction was stopped by moving the tubes to ice and washing the cells with PBS-EGG buffer. Cells were resuspended in PBS containing 0.1% BSA and activated rhodamine 123 signal (activated DHR 123) was analyzed in the FITC channel on a LSRII flow cytometer (BD) within 30 min. Hydrogen peroxide added to cells served as a positive control.

In vitro macrophage differentiation experiment

Monocytes and neutrophil were co-cultured to investigate if neutrophils can help to mature macrophages from their monocytic precursors. Neutrophils were FACS sorted based on cell surface marker expression (CD45$^+$CD11b$^+$Ly-6G$^+$SiglecF$^+$ or SiglecF$^-$) from lungs of KP1.9 tumor-bearing (T-SiglecF^{low} or T-SiglecF^{high}) or tumor-free mice (H-SiglecF^{low}) as detailed in the Flow cytometry methods section. Murine spleens were harvested from tumor-bearing mice and were used to enrich for monocytes. In detail, spleens were harvested, meshed through a 40 µm cell strainer and ACK lysed to remove erythrocytes. Splenic monocytes were enriched through a MACS based negative isolation protocol by incubating single cells with PE conjugated Abs specific for CD90.2, CD3, B220, CD19 and Ly-6G followed by anti-PE MACS beads. Both incubation steps were performed for 20min on ice. The negative isolation resulted in a 20-fold enrichment of monocytes based on flow cytometry measurements. This population likely also include myeloid precursors since these accumulate in spleens of tumor-bearing mice (*8*). For the co-culture, 4×10^4 monocytes and 8×10^4 neutrophils were incubated in Iscove's DMEM media supplemented with 10% FBS and 1% penicillin/streptomycin in 96-well cell culture plates for 6 days. Monocytes only and monocytes together with CSF-1 (1 µl/ml) were used as controls. Cells were removed from the plate and investigated by flow cytometry for F4/80 and CD11b expression in order to assess myeloid cell differentiation.

In vitro alkaline phosphatase assay for osteoblastic colony formation

To study whether tumor derived circulating factors can affect the osteogenic potential, osteoblastic colony formation was investigated after addition of serum pooled from individual mice that were either tumor-bearing or tumor-free. In some experiments tumor-free serum with or without sRAGE was added. Long bones (femur and tibia) and vertebrae of tumor-free C57BL/6 mice were harvested and flushed. Single cell suspensions were generated using 70 µm cell strainer and red blood cells removed in a ACK lysis step. Cells were counted and resuspended (4×10^7/ml) in osteogenic medium (DMEM supplemented with 10% FBS and 1% penicillin/streptomycin, 10 mM B-glycerophosphate and 50 µg/ml ascorbic acid). $4x10^6$ cells were transferred to 6

well cell culture plates and 200 µl serum from tumor-bearing or tumor-free mice added. Medium was refreshed every second day and non-adherent cells were removed. Cells were fixed after 9–10 days by adding 4% PFA for 8 min followed by 2 washing steps with H_2O and the alkaline phosphate substrate reaction (B5655, Sigma) according to manufactures procedure. As counter stain, Nucleofast Red (Polysciences, Inc) was used. The number of ALP positive colonies was evaluated by 2–3 independent persons in a blinded manner.

In vitro co-culture of hematopoietic precursors and bone marrow stromal cells +/− sRAGE

To test whether sRAGE altered neutrophil maturation from hematopoietic precursors via stromal cells, we performed co-culture experiments. In detail, 1×10^3 ST2 cells per well were cultured in 96 well plates for two days. Then, bone marrow was harvested from tumor-free mice and depleted of differentiated cells using negative MACS bead separation (Abs specific for B220, CD19, Ter119, CD11c, CD11b, NK1.1, Dx5, CD127, Ly-6G and CD90.2 were utilized). The flow-through was collected. The following conditions were tested: ST2 cells, with or without 1×10^4 lineage negative bone marrow cells, and with increased doses of sRAGE (namely: no sRAGE, 0.01 µg/ml, 0.1 µg/ml, 1 µg/ml). Neutrophil maturation was evaluated after three days by staining for CD11b, Ly-6G and CXCR2 surface expression using flow cytometry (*1*).

p53 recombined PCR for tumor cell detection

Detection of p53 recombined locus (only present in KP tumor cells after exposure to Cre recombinase) was used to survey bone and marrow tissues for KP tumor cell metastases. In brief, DNA was extracted from bone marrow or calvarial bone (after digestion) using DNeasy blood and tissue kit (Qiagen) according to manufacturer's instructions. KP1.9 tumor cells were used as positive control. Different DNA concentrations from KP1.9 tumor cells were used to determine PCR detection limit to <10 cells (with the estimate of ~6pg DNA/cell). DNA was isolated from Gel PCR products from a primary PCR run. A second PCR amplification run on these DNA samples was performed to detect low levels of DNA in the isolated tissues. The following primers were used: A: 5′ CAC AAA AAC AGG TTA AAC CCA G 3′; B: 5′ AGC ACA TAG GAG GCA GAG AC 3′; C: 5′ GAA GAC AGA AAA GGG GAG GG 3′. Following bands were amplified: p53 recombined 1lox: 612bp, WT band: 288bp and a background band: 400bp.

Real-time PCR for analysis of blood samples

Neutrophils from the blood of KP lung tumor-bearing or tumor-free mice were investigated in order to define whether these cells exhibited transcriptional characteristics of tumor-infiltrating $SiglecF^{high}$ cells outside the tumor microenvironment. Neutrophils were FACS sorted based on surface marker expression ($CD45^+$ $CD11b^+$ $Ly\text{-}6G^+$) and RNA was isolated from the sorted cells using the RNeasy Micro Kit (Qiagen) according to manufactures procedures. Afterwards, cDNA was generated utilizing the High Capacity cDNA Reverse Transcription Kit (Applied Biosystems) and Real time PCR assays performed using the TaqMan Fast Advanced MasterMix together with TaqMan probes at the 7500 Fast Real-Time PCR System (Applied Biosystems). β2-Microglobulin was used as a housekeeping gene.

Protein array

To investigate soluble factors in serum or plasma of KP and KP1.9 lung tumor-bearing or tumor-free control mice, a membrane-based sandwich immunoassay with 111 different cytokine and chemokine antibodies was performed using the Proteome Profiler Mouse XL Cytokine Array Kit (R&D Systems) according to manufactures procedures. The captured soluble factors were visualized in duplicate using a chemiluminescent detection readout with an exposure time of 3 min. The signal intensity from each protein spot on the array was quantified using the Microarray_ Profile plugin in FIJI (www.optinav.info/MicroArray_Profile.htm). The intensity was normalized against six reference spots on each array. From two independent experiments, fold change of tumor versus tumor-free soluble factors was calculated and the resulting values presented in a heat map. Factors below detection level and that failed to alter reproducibly were excluded from further analysis.

sRAGE ELISA

Mouse sRAGE levels in the serum of KP1.9 tumor-bearing or tumor-free mice were quantified using ELISA according to manufacturer's instructions (MRG00, R&D systems). OD values were measured at 450 and 570nm (reference value) using a Tecan microplate reader. Murine blood was harvested and transferred to BD Microtainer tubes, incubated at room temperature for 30 min, spun at 1000 g for 15 min and the serum was stored at −80°C until ELISA analysis. The concentration of sRAGE in serum samples, investigated in duplicate, was calculated by extrapolating values of a standard curve following manufactures guidelines.

Flow cytometry

Single cell suspensions were obtained from lung tumors, bone marrow, spleen and bone tissue. The respective tissues and isolated single cell fractions were kept on ice for all steps if not stated otherwise. Tumor tissue was received by dissecting out tumor-bearing lungs. Small tissue pieces were generated using scissors and digested (RPMI containing 0.2 mg/ml collagenase type I, Worthington Biochemical Corporation) for 1 h at 37°C while shaking. Femurs and for some experiments tibias were harvested, cleaned and the bone marrow flushed out using cold staining buffer (PBS containing 0.5% BSA and 2 mM EDTA). Digested lung tissue and harvested bone marrow were gently meshed through 40 µM cell strainers using a plunger. Spleens were harvested and also meshed through 40 µM cell strainer as described before. Red blood cells were removed using 1 ml ACK lysis buffer (Lonza) per cell pellet for 1 min (for lung cells) or 2 min (for spleen cells) and the reaction was stopped with RPMI media. In some experiments blood was collected from the cheek or if mice were euthanized via cardiac puncture and directly treated with 5 ml ACK lysis buffer for 5 min to remove red blood cells. The resulting single-cell suspensions were washed and resuspended in staining buffer. In order to investigate bone cells by flow cytometry, in general, long bones were harvested, cleaned and crushed gently and the released cells were collected (fraction 1) and lysed with ACK lysis buffer. In parallel, the bone fragments (fraction 2) were cut into small pieces with scissors, filtered through 70 µM cell strainer, digested (PBS containing 20% FBS and 0.25% collagenase type I) for 1 h at 37°C, washed and finally pooled with the cells derived from fraction 1.

Single cell suspensions were incubated with FcBlock (clone 93, Biolegend) for 15 min at 4°C, followed by staining with fluorescent conjugated Abs for 45 min at 4°C. The cells were washed with staining buffer and analyzed on a LSRII flow cytometer (BD). 7-aminoactinomycin (7AAD, Sigma) positivity was used to exclude dead cells. Flow Cytometry Absolute Count Standard (Bangs Laboratories) were used to quantify circulating neutrophils.

Following cell populations were identified based on cell marker expression: Ocn^+ cells (Lin^- $CD45^-$ $CD31^-$ $Ter119^-$ YFP^+), neutrophils ($CD45^+$ $CD11b^+$ $Ly\text{-}6G^+$), $SiglecF^{high}$ neutrophils ($CD45^+$ $CD11b^+$ $Ly\text{-}6G^+$ $SiglecF^{high}$), $SiglecF^{low}$ neutrophils ($CD45^+$ $CD11b^+$ $Ly\text{-}6G^+$ $SiglecF^{low}$), monocytes ($CD45^+$ $CD11b^+$ $Ly\text{-}6G^-$ $Ly\text{-}6C^{high}$), $CD11b^-$ alveolar macrophages ($CD45^+$ $CD11b^-$ $F4/80^+$ $SiglecF^+$ $CD11c^+$), $CD11b^+$ macrophage-like cells ($CD45^+$ $CD11b^+$ $Ly6G^-$ $Ly6C^-$), T cells ($CD45^+$ $CD3^+$ $CD4^+$ or $CD8^+$), B cells ($CD45^+$ $B220^+$ $CD19^+$), NK cells ($CD45^+$ $CD49b^+$ $NK1.1^+$ or $CD45^+$ $CD49b^+$ $NKp46^+$).

The lineage (Lin) Ab mix contained the following Abs unless otherwise noted: B220, CD19, Ter119, CD11c, CD11b, NK1.1, CD49b, CD127, Ly-6G, CD90.2.

Following Abs were purchased from BD if not mentioned differently: B220 (553089, clone RA3-6B2); CD19 (553786, clone 1D3); Ter119 (553673, clone TER-119); CD11c (12-0114-83, clone N418, eBioscience); CD11b (557397, clone M1/70); NK1.1 (553165, 550627, clone PK136); CD49b (553858, clone DX5); CD127 (12-1271-82, clone A7R34, eBioscience); Ly-6G (551461, 560599, clone 1A8); CD90.2 (553006, clone 53–2.1); SiglecF (564514, clone E50-2440); CD4 (557956, clone RM4-5), Biolegend: CD117 (105812, clone 2B8); F4/80 (123115, clone BM8); CD45.1 (110738, clone A20); CD45.2 (109831, clone 104); CD3e (100306, clone 145-2C11); CD8 (100725, clone 53.-6.7); CD19 (115530, clone 6D5); CD11c (117333, clone N418); Nkp46 (137619, clone 29A1.4); CD45 (103126, clone 30-F11); CXCR2/CD182 (149303, clone SA044G4) or R&D Systems: CLEC5a/MDL-1 (FAB1639P, clone 226402).

Statistical methods

Unpaired t-test was used to compare two groups. Multiple t-test was performed to compare several cell populations between two groups and false discovery rate was accounted for using the Benjamini–Hochberg–Yekutieli procedure with Q = 1%. One-way or Two-way ANOVA with subsequent post-hoc analysis was done to compare three or more groups. GraphPad Prism was used to test for statistical significance except for when noted. Matlab and Python were used for scRNA-seq analysis, corresponding statistical testing is described above in section 'Neutrophil single cell RNA-seq'. Python was used for patient survival analysis as detailed in section 'Bioinformatical analyses of lung adenocarcinoma patients'. *p < 0.05, **p < 0.01, ***p < 0.001, ****p < 0.0001, n.s. not significant.

REFERENCES AND NOTES

1. S. B. Coffelt, M. D. Wellenstein, K. E. de Visser, Neutrophils in cancer: Neutral no more. *Nat. Rev. Cancer* **16**, 431–446 (2016). doi: 10.1038/nrc.2016.52; pmid: 27282249
2. D. Hanahan, L. M. Coussens, Accessories to the crime: Functions of cells recruited to the tumor microenvironment. *Cancer Cell* **21**, 309–322 (2012). doi: 10.1016/j.ccr.2012.02.022; pmid: 22439926
3. D. I. Gabrilovich, S. Ostrand-Rosenberg, V. Bronte, Coordinated regulation of myeloid cells by tumours. *Nat. Rev. Immunol.* **12**, 253–268 (2012). doi: 10.1038/nri3175; pmid: 22437938
4. C. Engblom, C. Pfirschke, M. J. Pittet, The role of myeloid cells in cancer therapies. *Nat. Rev. Cancer* **16**, 447–462 (2016). doi: 10.1038/nrc.2016.54; pmid: 27339708
5. S. S. McAllister, R. A. Weinberg, The tumour-induced systemic environment as a critical regulator of cancer progression and metastasis. *Nat. Cell Biol.* **16**, 717–727 (2014). doi: 10.1038/ncb3015; pmid: 25082194
6. A.-J. Casbon *et al*., Invasive breast cancer reprograms early myeloid differentiation in the bone marrow to generate immunosuppressive neutrophils. *Proc. Natl. Acad. Sci. U.S.A.* **112**, E566–E575 (2015). doi: 10.1073/pnas.1424927112; pmid: 25624500
7. L. J. Bayne *et al*., Tumor-derived granulocyte-macrophage colony-stimulating factor regulates myeloid inflammation and T cell immunity in pancreatic cancer. *Cancer Cell* **21**, 822–835 (2012). doi: 10.1016/j.ccr.2012.04.025; pmid: 22698406
8. V. Cortez-Retamozo *et al*., Origins of tumor-associated macrophages and neutrophils. *Proc. Natl. Acad. Sci. U.S.A.* **109**, 2491–2496 (2012). doi: 10.1073/pnas.1113744109; pmid: 22308361
9. W.-C. Wu *et al*., Circulating hematopoietic stem and progenitor cells are myeloid-biased in cancer patients. *Proc. Natl. Acad. Sci. U.S.A.* **111**, 4221–4226 (2014). doi: 10.1073/pnas.1320753111; pmid: 24591638
10. A. J. Templeton *et al*., Prognostic role of neutrophil-to-lymphocyte ratio in solid tumors: A systematic review and meta-analysis. *J. Natl. Cancer Inst.* **106**, dju124 (2014). doi: 10.1093/jnci/dju124; pmid: 24875653
11. L. Jiang *et al*., Prognostic value of monocyte and neutrophils to lymphocytes ratio in patients with metastatic soft tissue sarcoma. *Oncotarget* **6**, 9542–9550 (2015). doi: 10.18632/oncotarget.3283; pmid: 25865224
12. S. H. Huang *et al*., Prognostic value of pretreatment circulating neutrophils, monocytes, and lymphocytes in oropharyngeal cancer stratified by human papillomavirus status. *Cancer* **121**, 545–555 (2015). doi: 10.1002/cncr.29100; pmid: 25336438
13. J. Hoggatt, Y. Kfoury, D. T. Scadden, Hematopoietic stem cell niche in health and disease. *Annu. Rev. Pathol.* **11**, 555–581 (2016). doi: 10.1146/annurev-pathol-012615-044414; pmid: 27193455
14. S. J. Morrison, D. T. Scadden, The bone marrow niche for haematopoietic stem cells. *Nature* **505**, 327–334 (2014). doi: 10.1038/nature12984; pmid: 24429631
15. A. Mendelson, P. S. Frenette, Hematopoietic stem cell niche maintenance during homeostasis and regeneration. *Nat. Med.* **20**, 833–846 (2014). doi: 10.1038/nm.3647; pmid: 25100529
16. M. R. Reagan, C. J. Rosen, Navigating the bone marrow niche: Translational insights and cancer-driven dysfunction. *Nat. Rev. Rheumatol.* **12**, 154–168 (2016). doi: 10.1038/nrrheum.2015.160; pmid: 26607387
17. L. M. Calvi *et al*., Osteoblastic cells regulate the haematopoietic stem cell niche. *Nature* **425**, 841–846 (2003). doi: 10.1038/nature02040; pmid: 14574413
18. A. Zaheer *et al*., In vivo near-infrared fluorescence imaging of osteoblastic activity. *Nat. Biotechnol.* **19**, 1148–1154 (2001). doi: 10.1038/nbt1201-1148; pmid: 11731784
19. R. Weissleder, M. J. Pittet, Imaging in the era of molecular oncology. *Nature* **452**, 580–589 (2008). doi: 10.1038/nature06917; pmid: 18385732
20. M. DuPage, A. L. Dooley, T. Jacks, Conditional mouse lung cancer models using adenoviral or lentiviral delivery of Cre recombinase. *Nat. Protoc.* **4**, 1064–1072 (2009). doi: 10.1038/nprot.2009.95; pmid: 19561589
21. C. Pfirschke *et al*., Immunogenic chemotherapy sensitizes tumors to checkpoint blockade therapy. *Immunity* **44**, 343–354 (2016). doi: 10.1016/j.immuni.2015.11.024; pmid: 26872698
22. G. Karsenty, H. M. Kronenberg, C. Settembre, Genetic control of bone formation. *Annu. Rev. Cell Dev. Biol.* **25**, 629–648 (2009). doi: 10.1146/annurev.cellbio.042308.113308; pmid: 19575648
23. J. Y. Wu, D. T. Scadden, H. M. Kronenberg, Role of the osteoblast lineage in the bone marrow hematopoietic niches. *J. Bone Miner. Res.* **24**, 759–764 (2009). doi: 10.1359/jbmr.090225; pmid: 19257832
24. M. Weinreb, D. Shinar, G. A. Rodan, Different pattern of alkaline phosphatase, osteopontin, and osteocalcin expression in developing rat bone visualized by in situ hybridization. *J. Bone Miner. Res.* **5**, 831–842 (1990). doi: 1614906510.1002/jbmr.5650050806; pmid: 2239367
25. I. Bilic-Curcic *et al*., Visualizing levels of osteoblast differentiation by a two-color promoter-GFP strategy: Type I collagen-GFPcyan and osteocalcin-GFPtpz. *Genesis* **43**, 87–98 (2005). doi: 10.1002/gene.20156; pmid: 16149065
26. A. Bozec *et al*., Fra-2/AP-1 controls bone formation by regulating osteoblast differentiation and collagen production. *J. Cell Biol.* **190**, 1093–1106 (2010). doi: 10.1083/jcb.201002111; pmid: 20837772
27. A. Bozec *et al*., Osteoblast-specific expression of Fra-2/AP-1 controls adiponectin and osteocalcin expression and affects metabolism. *J. Cell Sci.* **126**, 5432–5440 (2013). doi: 10.1242/jcs.134510; pmid: 24046454
28. B. M. Abdallah *et al*., DLK1 is a novel regulator of bone mass that mediates estrogen deficiency-induced bone loss in mice. *J. Bone Miner. Res.* **26**, 1457–1471 (2011). doi: 10.1002/jbmr.346; pmid: 21308776
29. K. Watari *et al*., Impaired differentiation of macrophage lineage cells attenuates bone remodeling and inflammatory angiogenesis in *Ndrg1* deficient mice. *Sci. Rep.* **6**, 19470 (2016). doi: 10.1038/srep19470; pmid: 26778110
30. J. R. Cubillos-Ruiz *et al*., ER stress sensor XBP1 controls anti-tumor immunity by disrupting dendritic cell homeostasis. *Cell* **161**, 1527–1538 (2015). doi: 10.1016/j.cell.2015.05.025; pmid: 26073941
31. Z. Ang, J. Z. Er, J. L. Ding, The short-chain fatty acid receptor *GPR43* is transcriptionally regulated by XBP1 in human monocytes. *Sci. Rep.* **5**, 8134 (2015). doi: 10.1038/srep08134; pmid: 25633224
32. J. Schmielau, O. J. Finn, Activated granulocytes and granulocyte-derived hydrogen peroxide are the underlying mechanism of suppression of t-cell function in advanced cancer patients. *Cancer Res.* **61**, 4756–4760 (2001). pmid: 11406548
33. S. Kusmartsev, Y. Nefedova, D. Yoder, D. I. Gabrilovich, Antigen-specific inhibition of $CD8^+$ T cell response by immature myeloid cells in cancer is mediated by reactive oxygen species. *J. Immunol.* **172**, 989–999 (2004). doi: 10.4049/jimmunol.172.2.989; pmid: 14707072
34. K. Shedden *et al*., Gene expression-based survival prediction in lung adenocarcinoma: A multi-site, blinded validation study. *Nat. Med.* **14**, 822–827 (2008). doi: 10.1038/nm.1790; pmid: 18641660
35. D. X. Nguyen *et al*., WNT/TCF signaling through LEF1 and HOXB9 mediates lung adenocarcinoma metastasis. *Cell* **138**, 51–62 (2009). doi: 10.1016/j.cell.2009.04.030; pmid: 19576624
36. A. M. Schmidt, Soluble RAGEs—Prospects for treating & tracking metabolic and inflammatory disease. *Vascul. Pharmacol.* **72**, 1–8 (2015). doi: 10.1016/j.vph.2015.06.011; pmid: 26130225
37. Z. Zhou, W. C. Xiong, RAGE and its ligands in bone metabolism. *Front. Biosci.* **3**, 768–776 (2011). pmid: 21196410
38. E. Lalla *et al*., Blockade of RAGE suppresses periodontitis-associated bone loss in diabetic mice. *J. Clin. Invest.* **105**, 1117–1124 (2000). doi: 10.1172/JCI8942; pmid: 10772656
39. N. Mercer, H. Ahmed, S. B. Etcheverry, G. R. Vasta, A. M. Cortizo, Regulation of advanced glycation end product (AGE) receptors and apoptosis by AGEs in osteoblast-like cells. *Mol. Cell. Biochem.* **306**, 87–94 (2007). doi: 10.1007/s11010-007-9557-8; pmid: 17660952
40. H. Nozawa, C. Chiu, D. Hanahan, Infiltrating neutrophils mediate the initial angiogenic switch in a mouse model of multistage carcinogenesis. *Proc. Natl. Acad. Sci. U.S.A.* **103**, 12493–12498 (2006). doi: 10.1073/pnas.0601807103; pmid: 16891410
41. F. Shojaei *et al*., Bv8 regulates myeloid-cell-dependent tumour angiogenesis. *Nature* **450**, 825–831 (2007). doi: 10.1038/nature06348; pmid: 18064003
42. M. Kowanetz *et al*., Granulocyte-colony stimulating factor promotes lung metastasis through mobilization of Ly6G+Ly6C+ granulocytes. *Proc. Natl. Acad. Sci. U.S.A.* **107**, 21248–21255 (2010). doi: 10.1073/pnas.1015855107; pmid: 21081700
43. Z. G. Fridlender *et al*., Polarization of tumor-associated neutrophil phenotype by TGF-β: "N1" versus "N2" TAN. *Cancer Cell* **16**, 183–194 (2009). doi: 10.1016/j.ccr.2009.06.017; pmid: 19732719
44. S. K. Wculek, I. Malanchi, Neutrophils support lung colonization of metastasis-initiating breast cancer cells. *Nature* **528**, 413 (2015). doi: 10.1038/nature16140; pmid: 26649828
45. S. B. Coffelt *et al*., IL-17-producing γδ T cells and neutrophils conspire to promote breast cancer metastasis. *Nature* **522**, 345–348 (2015). doi: 10.1038/nature14282; pmid: 25822788
46. A. J. Gentles *et al*., The prognostic landscape of genes and infiltrating immune cells across human cancers. *Nat. Med.* **21**, 938–945 (2015). doi: 10.1038/nm.3909; pmid: 26193342
47. D. I. Gabrilovich, Myeloid-derived suppressor cells. *Cancer Immunol. Res.* **5**, 3–8 (2017). doi: 10.1158/2326-6066.CIR-16-0297; pmid: 28052991
48. D. Visnjic *et al*., Conditional ablation of the osteoblast lineage in Col2.3Δtk transgenic mice. *J. Bone Miner. Res.* **16**, 2222–2231 (2001). doi: 10.1359/jbmr.2001.16.12.2222; pmid: 11760835
49. M. Zhang *et al*., Osteoblast-specific knockout of the insulin-like growth factor (IGF) receptor gene reveals an essential role of IGF signaling in bone matrix mineralization. *J. Biol. Chem.* **277**, 44005–44012 (2002). doi: 10.1074/jbc.M208265200; pmid: 12215457
50. D. Visnjic *et al*., Hematopoiesis is severely altered in mice with an induced osteoblast deficiency. *Blood* **103**, 3258–3264 (2004). doi: 10.1182/blood-2003-11-4011; pmid: 14726388
51. A. Greenbaum *et al*., CXCL12 in early mesenchymal progenitors is required for haematopoietic stem-cell maintenance. *Nature* **495**, 227–230 (2013). doi: 10.1038/nature11926; pmid: 23434756
52. L. Ding, S. J. Morrison, Haematopoietic stem cells and early lymphoid progenitors occupy distinct bone marrow niches. *Nature* **495**, 231–235 (2013). doi: 10.1038/nature11885; pmid: 23434755
53. J. Y. Wu *et al*., Osteoblastic regulation of B lymphopoiesis is mediated by $G_s\alpha$-dependent signaling pathways. *Proc. Natl. Acad. Sci. U.S.A.* **105**, 16976–16981 (2008). doi: 10.1073/pnas.0802898105; pmid: 18957542
54. J. Zhu *et al*., Osteoblasts support B-lymphocyte commitment and differentiation from hematopoietic stem cells. *Blood* **109**, 3706–3712 (2007). doi: 10.1182/blood-2006-08-041384; pmid: 17227831
55. V. W. C. Yu *et al*., Specific bone cells produce DLL4 to generate thymus-seeding progenitors from bone marrow. *J. Exp. Med.* **212**, 759–774 (2015). doi: 10.1084/jem.20141843; pmid: 25918341
56. K. Fulzele *et al*., Myelopoiesis is regulated by osteocytes through Gsα-dependent signaling. *Blood* **121**, 930–939 (2013). doi: 10.1182/blood-2012-06-437160; pmid: 23160461
57. M. H. G. P. Raaijmakers *et al*., Bone progenitor dysfunction induces myelodysplasia and secondary leukaemia. *Nature* **464**, 852–857 (2010). doi: 10.1038/nature08851; pmid: 20305640
58. A. Kode *et al*., Leukaemogenesis induced by an activating β-catenin mutation in osteoblasts. *Nature* **506**, 240–244 (2014). doi: 10.1038/nature12883; pmid: 24429522
59. A. E. Broadus *et al*., Humoral hypercalcemia of cancer. Identification of a novel parathyroid hormone-like peptide. *N. Engl. J. Med.* **319**, 556 (1988). doi: 10.1056/NEJM198809013190906; pmid: 3043221

60. R. Coleman, J. J. Body, M. Aapro, P. Hadji, J. Herrstedt, Bone health in cancer patients: ESMO clinical practice guidelines. *Ann. Oncol.* **25** (suppl. 3), iii124–iii137 (2014). doi: 10.1093/annonc/mdu103; pmid: 24782453
61. R. Rizzoli *et al*., Cancer-associated bone disease. *Osteoporos. Int.* **24**, 2929–2953 (2013) doi: 10.1007/s00198-013-2530-3; pmid: 24146095.
62. E. Pompe *et al*., Intravenous contrast injection significantly affects bone mineral density measured on CT. *Eur. Radiol.* **25**, 283–289 (2015). doi: 10.1007/s00330-014-3408-2; pmid: 25187384
63. S. Srinivas *et al*., Cre reporter strains produced by targeted insertion of *EYFP* and *ECFP* into the *ROSA26* locus. *BMC Dev. Biol.* **1**, 4 (2001). doi: 10.1186/1471-213X-1-4; pmid: 11299042
64. T. Buch *et al*., A Cre-inducible diphtheria toxin receptor mediates cell lineage ablation after toxin administration. *Nat. Methods* **2**, 419–426 (2005). doi: 10.1038/nmeth762; pmid: 15908920
65. M. L. Bouxsein *et al*., Guidelines for assessment of bone microstructure in rodents using micro-computed tomography. *J. Bone Miner. Res.* **25**, 1468–1486 (2010). doi: 10.1002/jbmr.141; pmid: 20533309
66. M. N. Wein *et al*., SIKs control osteocyte responses to parathyroid hormone. *Nat. Commun.* **7**, 13176 (2016). doi: 10.1038/ncomms13176; pmid: 27759007
67. E. S. Liu *et al*., 1,25-Dihydroxyvitamin D alone improves skeletal growth, microarchitecture, and strength in a murine model of XLH, despite enhanced FGF23 expression. *J. Bone Miner. Res.* **31**, 929–939 (2016). doi: 10.1002/jbmr.2783; pmid: 26751835
68. D. W. Dempster *et al*., Standardized nomenclature, symbols, and units for bone histomorphometry: A 2012 update of the report of the ASBMR histomorphometry nomenclature committee. *J. Bone Miner. Res.* **28**, 2–17 (2013). doi: 10.1002/jbmr.1805; pmid: 23197339
69. G. Courties *et al*., Ischemic stroke activates hematopoietic bone marrow stem cells. *Circ. Res.* **116**, 407–417 (2015). doi: 10.1161/CIRCRESAHA.116.305207; pmid: 25362208
70. F. Pucci *et al*., SCS macrophages suppress melanoma by restricting tumor-derived vesicle-B cell interactions. *Science* **352**, 242–246 (2016). doi: 10.1126/science.aaf1328; pmid: 26989197
71. A. M. Klein *et al*., Droplet barcoding for single-cell transcriptomics applied to embryonic stem cells. *Cell* **161**, 1187–1201 (2015). doi: 10.1016/j.cell.2015.04.044; pmid: 26000487
72. R. Zilionis *et al*., Single-cell barcoding and sequencing using droplet microfluidics. *Nat. Protoc.* **12**, 44–73 (2017). doi: 10.1038/nprot.2016.154; pmid: 27929523
73. T. S. Heng, M. W. Painter; Immunological Genome Project Consortium, The Immunological Genome Project: Networks of gene expression in immune cells. *Nat. Immunol.* **9**, 1091–1094 (2008). doi: 10.1038/ni1008-1091; pmid: 18800157
74. Y. Benjamini, Y. Hochberg, Controlling the false discovery rate: A practical and powerful approach to multiple testing. *J. R. Stat. Soc.* **57**, 289–300 (1995).
75. A. Subramanian *et al*., Gene set enrichment analysis: A knowledge-based approach for interpreting genome-wide expression profiles. *Proc. Natl. Acad. Sci. U.S.A.* **102**, 15545–15550 (2005). doi: 10.1073/pnas.0506580102; pmid: 16199517
76. V. K. Mootha *et al*., PGC-1alpha-responsive genes involved in oxidative phosphorylation are coordinately downregulated in human diabetes. *Nat. Genet.* **34**, 267–273 (2003). doi: 10.1038/ng1180; pmid: 12808457
77. M. Meredith, D. Zemmour, D. Mathis, C. Benoist, Aire controls gene expression in the thymic epithelium with ordered stochasticity. *Nat. Immunol.* **16**, 942 (2015). doi: 10.1038/ni.3247; pmid: 26237550
78. A. Gordon, G. J. Hannon, Fastx-toolkit, version 0.0.13 (2010); http://hannonlab.cshl.edu/fastx_toolkit/index.html
79. D. Kim *et al*., TopHat2: Accurate alignment of transcriptomes in the presence of insertions, deletions and gene fusions. *Genome Biol.* **14**, R36 (2013). doi: 10.1186/gb-2013-14-4-r36; pmid: 23618408
80. H. Li *et al*., The Sequence Alignment/Map format and SAMtools. *Bioinformatics* **25**, 2078–2079 (2009). doi: 10.1093/bioinformatics/btp352; pmid: 19505943
81. M. I. Love, W. Huber, S. Anders, Moderated estimation of fold change and dispersion for RNA-seq data with DESeq2. *Genome Biol.* **15**, 550 (2014). doi: 10.1186/s13059-014-0550-8; pmid: 25516281
82. J. A. Miller *et al*., Strategies for aggregating gene expression data: The collapseRows R function. *BMC Bioinformatics* **12**, 322 (2011). doi: 10.1186/1471-2105-12-322; pmid: 21816037
83. T. Therneau, *Survival analysis*, version **2.41-3** (2017); https://cran.r-project.org/web/packages/survival/index.html.
84. C. Davidson-Pilon, Lifelines. Survival analysis in Python (2016); https://github.com/CamDavidsonPilon/lifelines.

ACKNOWLEDGMENTS

We thank the Harvard Stem Cell Institute for help with FACS sorting; D. Brooks, M. Scott, and M. Bouxsein from the Center for Skeletal Research Core (NIH grant P30-AR066261) for μCT bone analysis services; members of the Hope Babette Tang Histology Facility at the Koch Institute Swanson Biotechnology Center for technical support; M. Wein for helpful discussions and technical assistance; and D. Mathis, C. Benoist, S. Pillai, S. McAllister, and G. Dranoff for their input. This work was supported in part by the Samana Cay MGH (Massachusetts General Hospital) Research Scholar Fund, the Robert Wenner Award from the Swiss Cancer League, and NIH grants R01-AI084880, R01-CA206890, and P50-CA86355 (to M.J.P.); NIH grant U54-CA126515 (to R.W.); NIH grant CA148180 (to D.T.S.); NIH grant U54-CA163109 and the Howard Hughes Medical Institute (to R.O.H.); NIH grant R33-CA212697 and an Edward J. Mallinckrodt Jr. Fellowship (to A.K.); Boehringer Ingelheim Fonds PhD fellowships (to C.E. and D.Z.); Deutsche Forschungsgemeinschaft PF809/1-1 and MGH ECOR (Executive Committee on Research) Tosteson Postdoctoral Fellowship (to C.P.); a postdoctoral fellowship from the MIT (Massachusetts Institute of Technology) Ludwig Center for Molecular Oncology Research (to S.R.); and award T32-GM007753 from the National Institute of General Medical Sciences (to O.K.Y.). A.K. is a founder of, and is on the Scientific Advisory Board of, 1CellBio. R.O.H. is a scientific advisor for Genentech and Amgen. M.J.P., C.E., and C.P. are inventors on patent application 62/489,118 filed by MGH that covers the detection and targeting of tumor-promoting neutrophils. Osteoblast RNA-seq data have been deposited to the GEO (Gene Expression Omnibus) repository under the accession number GSE104294.

SUPPLEMENTARY MATERIALS

www.sciencemag.org/content/358/6367/eaal5081/suppl/DC1
Figs. S1 to S23
Tables S1 to S8
Reference (*85*)

30 November 2016; resubmitted 16 August 2017
Accepted 17 October 2017
10.1126/science.aal5081

Science

Osteoblasts remotely supply lung tumors with cancer-promoting SiglecF^{high} neutrophils

Camilla Engblom, Christina Pfirschke, Rapolas Zilionis, Janaina Da Silva Martins, Stijn A. Bos, Gabriel Courties, Steffen Rickelt, Nicolas Severe, Ninib Baryawno, Julien Faget, Virginia Savova, David Zemmour, Jaclyn Kline, Marie Siwicki, Christopher Garris, Ferdinando Pucci, Hsin-Wei Liao, Yi-Jang Lin, Andita Newton, Omar K. Yaghi, Yoshiko Iwamoto, Benoit Tricot, Gregory R. Wojtkiewicz, Matthias Nahrendorf, Virna Cortez-Retamozo, Etienne Meylan, Richard O. Hynes, Marie Demay, Allon Klein, Miriam A. Bredella, David T. Scadden, Ralph Weissleder and Mikael J. Pittet

Science **358** (6367), eaal5081.
DOI: 10.1126/science.aal5081

A bona fide portrayal of tumor growth

Bone has a well-established role in advanced cancer. It provides a supportive microenvironment for the growth of metastatic cells that escape the primary tumor, which ultimately leads to loss of bone mass. Engblom *et al.* show that bone may also contribute to early-stage tumorigenesis through a mechanism that leads to an increase in bone mass (see the Perspective by Zhang and Lyden). In mouse models of lung adenocarcinoma, primary tumor cells remotely activated bone-resident cells called osteoblasts, which have a bone-building function. The activated osteoblasts in turn triggered production of a certain type of neutrophil that infiltrates the primary tumor and promotes its growth. Patients with early-stage lung cancer were also found to have an increase in bone density, consistent with the findings in mice.

Science, this issue p. eaal5081; see also p. 1127